



PERGAMON

Journal of the Mechanics and Physics of Solids
50 (2002) 1469–1510

JOURNAL OF THE
MECHANICS AND
PHYSICS OF SOLIDS

www.elsevier.com/locate/jmps

Hydride-induced embrittlement and fracture in metals—effect of stress and temperature distribution

A.G. Varias^{a,b,*}, A.R. Massih^{a,c}

^aMaterials Science, Technology and Society, Malmö University, SE 205 06, Malmö, Sweden

^bSolid Mechanics Research Office, Makedonias 17, N. Iraklio 141 21, Athens, Greece

^cQuantum Technologies AB, Uppsala Science Park, SE-751 83, Uppsala, Sweden

Received 5 April 2001; received in revised form 10 September 2001; accepted 12 September 2001

Abstract

A mathematical model for the hydrogen embrittlement of hydride forming metals has been developed. The model takes into account the coupling of the operating physical processes, namely: (i) hydrogen diffusion, (ii) hydride precipitation, (iii) non-mechanical energy flow and (iv) hydride/solid-solution deformation. Material damage and crack growth are also simulated by using de-cohesion model, which takes into account the time variation of energy of de-cohesion, due to the time-dependent process of hydride precipitation. The bulk of the material, outside the de-cohesion layer, is assumed to behave elastically. The hydrogen embrittlement model has been implemented numerically into a finite element framework and tested successfully against experimental data and analytical solutions on hydrogen thermal transport (in: Wunderlich, W. (Ed.), Proceedings of the European Conference on Computational Mechanics, Munich, Germany, 1999, J. Nucl. Mater. (2000a) 279 (2–3) 273). The model has been used for the simulation of Zircaloy-2 hydrogen embrittlement and delayed hydride cracking initiation in (i) a boundary layer problem of a semi-infinite crack, under mode I loading and constant temperature, and (ii) a cracked plate, under tensile stress and temperature gradient. The initial and boundary conditions in case (ii) are those encountered in the fuel cladding of light water reactors, during operation. The effects of near-tip stress intensification as well as of temperature gradient on hydride precipitation and material damage have been studied. The numerical simulation predicts hydride precipitation at a small distance from the crack-tip. When the remote loading is sufficient, the near-tip hydrides fracture. Thus a microcrack is generated, which is separated from the main crack by a ductile ligament, in agreement with experimental observations. © 2002 Elsevier Science Ltd. All rights reserved.

*Corresponding author. Materials Science, Technology and Society, Malmö University, SE-205 06 Malmö, Sweden. Tel.: +46-40-665-7704, mobile: +46-709-315326; fax: +46-40-665-7135.

E-mail address: andreas.varias@ts.mah.se (A.G. Varias).

URL: <http://www.ts.mah.se/person/anva/>

Keywords: Hydride; Hydrogen; Embrittlement; Crack propagation; Cohesive zone; Chemo-mechanical processes

1. Introduction

The stimulation of the present study is coming from nuclear industry, where zirconium alloys are used in several structural parts of a nuclear reactor core. Although zirconium alloys have good mechanical properties, hydrogen embrittlement occurs during service at extended fuel burnup (usage) and may lead to significant reduction in fracture toughness (e.g. Coleman and Hardie, 1966). Indeed, hydrogen is generated due to the oxidation of zirconium by the coolant water in the reactor. Subsequently, it diffuses in the material and forms hydrides, when its terminal solid solubility is exceeded. The hydride is a brittle phase, which actually causes the embrittlement of the material. For this reason experimental and theoretical studies have been performed, early in the sixties and later on, in order to understand and simulate hydrogen diffusion and hydride formation in a zirconium alloy, under conditions encountered in the nuclear reactor core, where temperature gradient develops (Sawatzky, 1960; Markowitz, 1961; Sawatzky and Vogt, 1963; Marino, 1972).

The embrittlement of zirconium, due to hydride formation, may lead to delayed hydride cracking, a subcritical crack growth mechanism. This mechanism allows crack propagation to proceed in a discontinuous fashion; a complete crack growth cycle includes stress-directed diffusion of hydrogen towards the crack-tip, hydride formation and fracture. Delayed hydride cracking was observed in industrial applications (e.g. Northwood and Kosasih, 1983). For this reason, mathematical simulations were performed and important experimental data for zirconium alloys were obtained (e.g. Dutton et al., 1977; Coleman and Ambler, 1977; Huang and Mills, 1991; Efsing and Pettersson, 1996; Lufrano and Sofronis, 2000). The experimental measurements include the threshold stress intensity factor and the stage II crack growth rate for delayed hydride cracking.

Hydrogen embrittlement, caused by the formation of hydrides at stress concentration locations, has been also observed in electron-microscope studies of vanadium, niobium and titanium (Takano and Suzuki, 1974; Birnbaum et al., 1976; Grossbeck and Birnbaum, 1977; Shih et al., 1988).

The hydride-induced embrittlement is a complicated mechanism, which results from the simultaneous operation of several coupled processes, namely, (i) hydrogen diffusion, (ii) hydride precipitation, (iii) non-mechanical energy flow, and (iv) material deformation. Note that hydrogen diffusion is driven by chemical potential and temperature gradients (e.g. Denbigh, 1951; Shewmon, 1989). Hydrogen chemical potential depends on stress (Li et al., 1966) and therefore hydrogen diffusion is coupled with material deformation and non-mechanical energy flow. The hydrogen terminal solid solubility also depends on temperature as well as on stress, due to hydride expansion during precipitation (e.g. Birnbaum et al., 1976; Puls, 1981), leading to the coupling of hydride precipitation with material deformation and non-mechanical energy flow.

Finally, material deformation depends on all other processes due to material expansion, which is caused by hydrogen dissolution (Peisl, 1978), hydride formation and temperature increase. A model for hydride-induced embrittlement, which takes into account the coupling of the operating processes, under constant temperature, has been developed by Lufrano et al. (1996, 1998). In the present study the process of non-mechanical energy flow has also been considered, due to its importance in the degradation of nuclear fuel cladding, during reactor operation (e.g. Forsberg and Massih, 1990). For this purpose the thermodynamic theory of irreversible processes is considered (Denbigh, 1951) and hydrogen thermal transport (Sorét effect) is taken into account. Also crack growth initiation, due to delayed hydride cracking, has been simulated by developing a new version of de-cohesion model, which takes into account the time variation of energy of de-cohesion, due to the time-dependent process of hydride precipitation.

The model has been applied to the simulation of Zircaloy-2 hydrogen embrittlement (Varias and Massih, 1999, 2000a,c, 2001). It has been tested successfully against Sawatzky (1960) experiment and analytical solutions on hydrogen diffusion and hydride precipitation under stress and temperature gradients (Varias and Massih, 1999, 2000a). In the present investigation, the simulation of material degradation and crack growth initiation is discussed for (i) a boundary layer problem of a semi-infinite crack, under mode I loading and constant temperature, and (ii) a cracked plate, under tensile stress and temperature gradient. The initial and boundary conditions in case (ii) are those encountered in the fuel cladding of light water reactors, during operation.

The structure of the paper is the following. In Section 2 the mathematical model for hydride-induced embrittlement and fracture is presented for a metal/hydrogen system. More precisely, the thermodynamics of irreversible processes are briefly discussed. Details on the derivation of the thermodynamic forces, which drive hydrogen diffusion and non-mechanical energy flow, are given in Appendix A. In Sections 2.1, 2.2 and 2.3, the governing equations for hydrogen diffusion, non-mechanical energy flow and hydride precipitation are discussed. The constitutive relations for elastic material deformation are given in Section 2.4. The de-cohesion model is presented in Section 2.5. The numerical implementation of the model in a finite element framework is discussed in Appendix B. The application of the embrittlement model to Zircaloy-2 is presented in Section 3. In Section 3.1 the simulation of hydride precipitation and fracture ahead of a crack, under mode-I K-field dominance and constant temperature, is presented. The degradation of a cracked plate under conditions, encountered in nuclear fuel cladding, during reactor operation, is given in Section 3.2. Finally, concluding remarks are made in Section 4.

2. Mathematical model for hydride precipitation and fracture

In this section the governing equations for all operating processes are derived. The model is developed for a metal, M , which forms hydrides of the type MH_x . It could be niobium, titanium, vanadium or zirconium, which form hydrides of the type NbH , $TiH_{1.5}$, $VH_{0.5}$, and ZrH or $ZrH_{1.66}$, respectively. The presence of the hydrides is described by the hydride volume fraction; the hydrides are smeared. The development of

regions rich in hydrides, their shape and size is given by the distribution of hydride volume fraction. A version of the model, which is valid for zirconium alloys, has been discussed by Varias (1998a) and Varias and Massih (1999, 2000a).

Energy flow and diffusion of mass are coupled processes. A temperature gradient leads to flow of matter and therefore to a concentration gradient. Conversely, a diffusion process gives rise to a small temperature difference. A detailed discussion and relevant references for the thermodynamic treatment of energy-flow/diffusion as well as of other coupled phenomena are presented by Denbigh (1951). His treatise for irreversible processes is based on Onsager's principle of microscopic reversibility. In the following, the theory is applied to the processes of hydrogen diffusion and energy flow, occurring within hydride forming metals, under stress and temperature gradient.

According to the empirical law of Fourier, heat flux is linearly related to the temperature gradient, which is the thermodynamic force, driving heat flow. In the case of diffusion the classical Fick's law has been modified. In an isothermal system, the flux of a diffusing substance is proportional to the gradient of its chemical potential. Then, chemical potential gradient is the thermodynamic force driving diffusion under isothermal conditions. When the processes operate simultaneously, the coupling is taken into account by assuming that the non-mechanical energy and hydrogen fluxes are linearly related to both thermodynamic forces:

$$J_i^E = L^E X_i^E + L^{EH} X_i^H, \quad (2.1a)$$

$$J_i^H = L^{HE} X_i^E + L^H X_i^H, \quad (2.1b)$$

$$L^{EH} = L^{HE}. \quad (2.1c)$$

J_i^E and J_i^H are the components of the non-mechanical energy flux and the hydrogen flux, respectively. It is noted that the energy flux includes conducted heat, described by Fourier's law, and the energy transported by the diffusing hydrogen. X_i^E and X_i^H are the thermodynamic forces driving non-mechanical energy flow and hydrogen diffusion, respectively. L^E , L^H , L^{EH} and L^{HE} are phenomenological coefficients. Relation (2.1c) is valid due to Onsager's reciprocity relation.

The thermodynamic forces are related to the gradients of the absolute temperature, T , and the chemical potential of hydrogen in the solid solution, μ^H :

$$X_i^E = -\frac{1}{T} \frac{\partial T}{\partial x_i}, \quad (2.2a)$$

$$X_i^H = -T \frac{\partial}{\partial x_i} \left(\frac{\mu^H}{T} \right). \quad (2.2b)$$

Their definition satisfies the following relation for the rate of internal generation of entropy per unit volume, ψ , caused by hydrogen diffusion and non-mechanical energy flow:

$$T\psi = J_i^E X_i^E + J_i^H X_i^H. \quad (2.3)$$

In Appendix A, the thermodynamic forces, (2.2), are derived, for the case of a metal under stress, where hydride precipitation may occur. Note that, as shown in Appendix A, hydride precipitation, under conditions of chemical equilibrium, does not contribute to the internal generation of entropy. This is also in agreement with a special case, which is discussed by Denbigh (1951); if a chemical reaction occurs under chemical equilibrium, in a material under constant temperature and pressure, it does not contribute to the internal generation of entropy.

2.1. Hydrogen diffusion under chemical potential and temperature gradients

When hydrogen and metal form a solid solution, the hydrogen flux satisfies the following relation (e.g. Shewmon, 1989):

$$J_k^{H,SS} = - \frac{D^H C^H}{RT} \left(\frac{\partial \mu^H}{\partial x_k} + \frac{Q^H}{T} \frac{\partial T}{\partial x_k} \right), \quad (2.4)$$

where R is the gas constant. Also C^H , D^H and Q^H are the concentration, the diffusion coefficient and the heat of transport of hydrogen in the metal, respectively. The concentration of hydrogen as well as the concentrations of other components or phases are given in moles per unit volume. Relation (2.4) is a special case of Eq. (2.1) and therefore valid for a metal under stress. Note that the effect of stress gradient on hydrogen diffusion is included in the chemical potential term, according to the discussion in Section 2.3.

Hydrogen diffusion in the hydride is significantly slower and therefore it can be neglected. Then, the total hydrogen flux in a hydride/solid-solution composite is given by the following relation:

$$J_k^H = (1 - f) J_k^{H,SS}, \quad (2.5)$$

where f is the volume fraction of the hydride in the material.

Mass conservation requires that the rate of total hydrogen concentration, C^{HT} , inside a volume V , is equal to the rate of hydrogen flowing through the boundary S :

$$\frac{d}{dt} \int_V C^{HT} dV + \int_S J_k^H n_k dS = 0. \quad (2.6)$$

Relation (2.6) is valid for an arbitrary volume. Then, one may derive the respective differential equation, by using divergence theorem:

$$\frac{dC^{HT}}{dt} = - \frac{\partial J_k^H}{\partial x_k}. \quad (2.7)$$

Note that the total hydrogen concentration, C^{HT} , is related to the concentration of hydrogen in the solid solution, C^H , and the hydride, $C^{H,hr}$, as follows:

$$C^{HT} = f C^{H,hr} + (1 - f) C^H. \quad (2.8)$$

C^H is defined with respect to the volume occupied by solid solution, i.e. $(1 - f)V$. C^H is equal to the hydrogen terminal solid solubility, C^{TS} , when $f \neq 0$. Similarly, $C^{H,hr}$ is

defined with respect to the volume occupied by the hydride, i.e. fV , and therefore it can be considered constant, independent of temperature.

Note that, in the hydrogen diffusion model, the effect of hydrogen trapping in the solid solution by dislocations and voids, has been neglected, since the bulk of the material is assumed to behave elastically. However, the effect of traps is more important at low temperatures, where the lattice solubility is relatively small (e.g. Shewmon, 1989). The temperatures, under consideration in the present study, are about equal to or larger than 300°C.

2.2. Non-mechanical energy flow due to heat conduction and hydrogen diffusion

The first step for the derivation of the differential equation, which governs non-mechanical energy flow, is the determination of energy flux. Consequently, according to the general relations (2.1), the phenomenological coefficients L^E and L^{EH} need to be determined. Initially, hydrogen/metal solid solution is considered. Comparison of relations (2.4), (2.1b, c) and (2.2a, b) leads to the determination of the coefficients L^H and L^{EH} :

$$L^H = \frac{D^H C^H}{RT}, \quad (2.9a)$$

$$L^{HE} = L^{EH} = \frac{D^H C^H}{RT} (Q^H + \mu^H). \quad (2.9b)$$

The remaining coefficient L^E can be determined, by taking into account the well known empirical law of Fourier for heat conduction:

$$J_i^E = -k \frac{\partial T}{\partial x_i}, \quad (2.10)$$

where k is the thermal conductivity of the metal. Note that relation (2.10) is valid, when there is no hydrogen diffusion. Therefore, Eq. (2.10) is valid when:

$$\frac{\partial \mu^H}{\partial x_i} = -\frac{Q^H}{T} \frac{\partial T}{\partial x_i}. \quad (2.11)$$

By substituting Eqs. (2.10), (2.11) and (2.2a, b) into Eq. (2.1a), one may derive L^E :

$$L^E = kT + \frac{D^H C^H}{RT} (Q^H + \mu^H)^2. \quad (2.12)$$

All the coefficients of the phenomenological equations (2.1a, b) have been determined. Consequently, one may derive the expression for energy flux in a hydrogen/metal solid solution, simply by substituting Eqs. (2.9) and (2.12) into Eq. (2.1a) and taking into account relation (2.4) for hydrogen flux:

$$J_i^{E,SS} = (Q^H + \mu^H) J_i^{H,SS} - k \frac{\partial T}{\partial x_i}. \quad (2.13)$$

The first term of the right-hand side is the energy flux, which is produced by the diffusion of hydrogen atoms. The second term is the conducted heat. According to Eq. (2.13), the hydrogen heat of transport is the heat flux per unit flux of hydrogen in the

absence of temperature gradient. Q^H contributes to the variation of entropy, as shown in Appendix A (see relations (A.8)–(A.10)).

Hydrogen diffusion in the hydride is negligible (see Section 2.1) and, consequently, the flow of energy in the hydride is only due to heat conduction. It is assumed that the thermal conductivity of the hydride equals the thermal conductivity of the metal. Then, the following relation provides the total energy flux in the solid-solution/hydride composite:

$$J_i^E = (1 - f)J_i^{E,SS} - fk \frac{\partial T}{\partial x_i}, \quad (2.14a)$$

which when combined with Eqs. (2.5) and (2.13) leads to:

$$J_i^E = (Q^H + \mu^H)J_i^H - k \frac{\partial T}{\partial x_i}. \quad (2.14b)$$

In order to completely describe the process of energy flow, the conservation of energy should be enforced. Energy conservation requires that the internal energy rate equals the energy input rate due to the external stress power and the non-mechanical energy flow, (e.g. Malvern, 1969):

$$\rho \frac{du}{dt} = \sigma_{ij} \frac{d\varepsilon_{ij}}{dt} - \frac{\partial J_k^E}{\partial x_k}, \quad (2.15)$$

where ρ , u , σ_{ij} and ε_{ij} are the mass density of the material, the internal energy per unit mass, the stress tensor and the strain tensor, respectively. The minus sign, in Eq. (2.15), is due to the convention that the energy flux is positive when it leaves the body. According to the discussion in Appendix A, continuum thermodynamics, based on a caloric equation of state, also relates internal energy with specific entropy, s , total hydrogen concentration and other sub-state variables:

$$\rho \frac{du}{dt} = \rho T \frac{ds}{dt} + \sigma_{ij} \frac{d\varepsilon_{ij}}{dt} + \mu^H \frac{dC^{HT}}{dt}. \quad (2.16)$$

Manipulation of relations (2.7), (2.15) and (2.16) leads to the following differential equation:

$$\rho T \frac{ds}{dt} = \frac{\partial}{\partial x_i} \left(k \frac{\partial T}{\partial x_i} \right) - Q^H \frac{\partial J_m^H}{\partial x_m} - J_n^H \frac{\partial \mu^H}{\partial x_n}. \quad (2.17)$$

Entropy rate is also related to the rates of temperature, hydride volume fraction and total hydrogen concentration. This relation is derived by taking into account the dependence of entropy on all thermodynamic variables (i.e. temperature, stress as well as hydride, metal and hydrogen concentrations):

$$\rho T \frac{ds}{dt} = \rho c_p \frac{dT}{dt} + \frac{\Delta \tilde{H}^{hr}}{\bar{V}^{hr}} \frac{df}{dt} + Q^H \frac{dC^{HT}}{dt}, \quad (2.18)$$

where c_p is the specific heat of the metal at constant pressure, $\Delta \tilde{H}^{hr}$ is the enthalpy associated with the formation of a mole of hydride and \bar{V}^{hr} is the hydride molal

volume. In deriving Eq. (2.18), the following are taken into account: (i) The total number of moles of the metal in solid solution and in hydride remains constant. (ii) The partial derivative of entropy with respect to temperature is related to the specific heat of the solid solution/hydride material under constant stress, $c_\sigma = T(\partial s/\partial T)_\sigma$. In the present analysis c_σ is assumed to be equal to c_p . (iii) At the level of approximation of neglecting thermoelastic coupling, the partial derivative of entropy with respect to stress is taken equal to zero. Note that, in metals and ceramics, thermoelastic coupling effects are quite small (Boley and Wiener, 1960). (iv) The change of entropy due to hydride formation is equal to $\Delta\bar{H}^{\text{hr}}/T$. (v) The change of entropy due to the addition of a mole of hydrogen in the solid solution is equal to Q^{H}/T .

Substitution of Eq. (2.18) into Eq. (2.17) leads to the differential equation, which governs the flow of non-mechanical energy:

$$\rho c_p \frac{dT}{dt} + \frac{\Delta\bar{H}^{\text{hr}}}{\bar{V}^{\text{hr}}} \frac{df}{dt} = \frac{\partial}{\partial x_i} \left(k \frac{\partial T}{\partial x_i} \right) - J_n^{\text{H}} \frac{\partial \mu^{\text{H}}}{\partial x_n}. \quad (2.19)$$

Therefore, the variation of the heat content in the metal–hydride composite depends on conducted heat, heat generated during hydrogen diffusion and heat released during hydride formation.

2.3. Terminal solid solubility of hydrogen in a metal under stress

According to the mathematical formulation for hydrogen diffusion and energy flow, discussed in previous sections, the knowledge of hydrogen chemical potential and terminal solid solubility is necessary. Both quantities depend on applied stress. The relations for these quantities are derived in the following.

The chemical potentials of mobile and immobile components in stressed solids have been derived by Li et al. (1966). According to their study, the chemical potential of a component B is given by the following relation:

$$\mu^{\text{B}} = \mu^{\text{B},0} + \frac{\partial w}{\partial N^{\text{B}}} - W^{\text{B}}, \quad (2.20)$$

where $\mu^{\text{B},0}$ is the chemical potential of component B, under stress-free conditions, for the same concentration as that under stress, w is the strain energy of the solid and N^{B} is the number of B moles. Therefore, the second term in the right-hand side of Eq. (2.20), $\partial w/\partial N^{\text{B}}$, represents the strain energy of the solid per mole of component B; in deriving $\partial w/\partial N^{\text{B}}$ the temperature and stress are being held constant. Finally, W^{B} is the work performed by the applied stresses, σ_{ij} , per mole of addition of component B. For immobile components, since the addition or removal of the component takes place at an external surface or an interface, the chemical potential is considered as a surface property. This is not the case for mobile components. For more details on the significance of the above comments and the respective derivations, the reader is referred to the article by Li et al. (1966).

Relation (2.20) is applied to a hydrogen/metal solid solution under stress. A material particle of volume, V , under uniform stress is considered:

$$\begin{aligned}\frac{\partial w}{\partial N^H} &= \frac{\partial}{\partial N^H} \left(\int_0^{\varepsilon_{mn}} V \sigma_{ij} d\varepsilon_{ij} \right) = \frac{\partial}{\partial N^H} \left(\int_0^{\sigma_{mn}} V \sigma_{ij} M_{ijkl} d\sigma_{kl} \right) \\ &= \int_0^{\sigma_{mn}} \left(\frac{\partial V}{\partial N^H} M_{ijkl} \sigma_{ij} + \frac{\partial M_{ijkl}}{\partial \chi^H} \frac{\partial \chi^H}{\partial N^H} V \sigma_{rs} \right) d\sigma_{kl}.\end{aligned}\quad (2.21)$$

M_{ijkl} is the elastic compliance tensor of the metal and χ^H is the mole fraction of hydrogen in the solid solution. The work performed by the applied stresses per mole of addition of hydrogen is given by the following relation:

$$W^H = V \sigma_{ij} \frac{\partial \varepsilon_{ij}}{\partial N^H} = V \sigma_{kk} \frac{\bar{V}^H}{3V} = \frac{\sigma_{kk}}{3} \bar{V}^H. \quad (2.22)$$

Substitution of Eqs. (2.21) and (2.22) into Eq. (2.20) leads to the final expression for the chemical potential of hydrogen, being in solid solution under stress:

$$\mu^H = \mu^{H,0} + \bar{V}^H \left(\frac{1}{2} M_{ijkl} \sigma_{ij} \sigma_{kl} - \frac{1}{3} \sigma_{mm} \right). \quad (2.23)$$

In deriving Eq. (2.23), it has been taken into account that the derivative of volume with respect to hydrogen moles equals the partial molal volume of hydrogen, \bar{V}^H . It has been also assumed that there is no effect of hydrogen on the elastic moduli of the material. Consequently, the derivative of the elastic compliance with respect to the mole fraction of hydrogen is equal to zero. Note that the first term in parenthesis in Eq. (2.23) is of the order of σ^2/E , where E is the elastic modulus of the metal. The second term is of the order of σ . Therefore, the second term is significantly larger than the first one. If the first term in parenthesis in Eq. (2.23) is neglected, a relation is derived, which is more often used in the literature.

The above relations for the chemical potential of mobile and immobile components are used, in the following, for the derivation of hydrogen terminal solid solubility in a metal under stress.

According to Eq. (2.20), hydride chemical potential, in a stressed material, is given by

$$\mu^{\text{hr}} = \mu^{\text{hr},0} + \frac{\partial w}{\partial N^{\text{hr}}} - W^{\text{hr}}, \quad (2.24a)$$

$$\frac{\partial w}{\partial N^{\text{hr}}} = \bar{w}_{\text{acc}} + \bar{w}_{\text{int}} + \bar{w}_{\text{af}}, \quad (2.24b)$$

$$\bar{w}_{\text{acc}} = -\frac{1}{2} \int_{\bar{V}^{\text{hr}}} \sigma_{ij}^I \varepsilon_{ij}^T dV, \quad (2.24c)$$

$$\bar{w}_{\text{int}} = -\int_{\bar{V}^{\text{hr}}} \sigma_{ij} \varepsilon_{ij}^T dV, \quad (2.24d)$$

$$\bar{w}_{\text{af}} = \frac{1}{2} \int_{\bar{V}^{\text{hr}}} \sigma_{ij} \varepsilon_{ij} dV, \quad (2.24e)$$

$$W^{\text{hr}} = \sigma_n \bar{V}^{\text{hr}}. \quad (2.24f)$$

In deriving relations (2.24) it was taken into account that hydride formation is accompanied by a deformation, ε_{ij}^T , which is mainly a volume expansion. Under no external loading, the above deformation leads to the development of stresses, σ_{ij}^I , in the hydride. Under no external loading, material strain energy per mole of precipitating hydride is given by Eq. (2.24c), while under externally applied stress, σ_{ij} , the interaction energy (2.24d) as well as the strain energy of the applied field (2.24e), should be also taken into account (Eshelby, 1957). In Eq. (2.24f) σ_n is the normal stress at the location of solid solution/hydride interface, where the chemical potential is considered.

The chemical potential of the stressed metal is defined as follows:

$$\mu^M = \mu^{M,0} + \frac{\partial w}{\partial N^M} - W^M, \quad (2.25a)$$

$$\frac{\partial w}{\partial N^M} = \frac{1}{2} \int_{\bar{V}^M} \sigma_{ij} \varepsilon_{ij} dV, \quad (2.25b)$$

$$W^M = \sigma_n \bar{V}^M, \quad (2.25c)$$

where \bar{V}^M is the volume of a mole of metal.

The hydride, MH_x , is assumed to be in equilibrium with hydrogen and metal either under stress or under stress-free conditions. Consequently,

$$\mu^{hr} = \mu^M + x\mu^H(C^{TS}), \quad (2.26a)$$

$$\mu^{hr,0} = \mu^{M,0} + x\mu^{H,0}(C^{TS,0}). \quad (2.26b)$$

$C^{TS}, C^{TS,0}$ are the values of hydrogen terminal solid solubility under applied stress and stress-free conditions, respectively. By substitution of relations (2.24), (2.25) and (2.26b) into Eq. (2.26a), one may derive:

$$\begin{aligned} & x[\mu^H(C^{TS}) - \mu^{H,0}(C^{TS,0})] \\ &= \bar{w}_{acc} + \bar{w}_{int} + \frac{1}{2} \left(\int_{\bar{V}^{hr}} \sigma_{ij} \varepsilon_{ij} dV - \int_{\bar{V}^M} \sigma_{kl} \varepsilon_{kl} dV \right) - \sigma_n(\bar{V}^{hr} - \bar{V}^M). \end{aligned} \quad (2.27)$$

It has been implied that hydride and metal equilibrium concentrations do not change significantly with stress. Because of material continuity, the molal volume of the hydride equals that of the solid solution at the hydride/solid-solution interface; consequently $\bar{V}^{hr} \approx \bar{V}^M$ and the terms of Eq. (2.27) in parenthesis vanish. Also in ideal or dilute solutions (Raoult's law), the stress-free hydrogen chemical potential satisfies the following well-known relation:

$$\mu^{H,0} = \mu^{H,RS} + RT \ln(C^H \bar{V}), \quad (2.28)$$

where $\mu^{H,RS}$ is hydrogen chemical potential in the 'standard' (i.e. reference) state and \bar{V} is the molal volume of solid solution. Then, by invoking Eq. (2.28) and substituting Eq. (2.23) into Eq. (2.27), one may derive the terminal solid solubility of hydrogen

in the metal under stress:

$$C^{\text{TS}} = C^{\text{TS},0} \exp\left(\frac{\bar{w}_{\text{acc}} + \bar{w}_{\text{int}}}{xRT}\right) \exp\left[\frac{\bar{V}^{\text{H}}}{RT} \left(\frac{\sigma_{mm}}{3} - \frac{1}{2} M_{ijkl} \sigma_{ij} \sigma_{kl}\right)\right]. \quad (2.29)$$

The above derivation is based on similar arguments, by Li et al. (1966), for the formation of cementite in ferrite. When the compliance term is neglected, Eq. (2.29) leads to the hydrogen terminal solid solubility derived by Puls (1981). In the numerical calculations, which are presented in following sections, the compliance terms of Eqs. (2.23) and (2.29) are neglected. Use of Eq. (2.29) or its simplified version, implies that chemical equilibrium occurs, under the local conditions of temperature and stress.

2.4. Hydride—solid solution deformation

In the present mathematical formulation all material phases are taken as elastic. It is also assumed that the elastic properties of the hydride and the solid solution are identical and do not depend on hydrogen concentration. The same assumption has been made in previous studies on hydride-induced embrittlement (e.g. Shi and Puls, 1994; Lufrano et al., 1996).

The material deformation is coupled with hydrogen diffusion and energy flow due to the strains, which are caused by hydrogen dissolution, hydride formation and thermal expansion:

$$\frac{d\sigma_{ij}}{dt} = M_{ijkl}^{-1} \left(\frac{d\epsilon_{kl}}{dt} - \frac{d\epsilon_{kl}^{\text{H}}}{dt} - \frac{d\epsilon_{kl}^{\text{E}}}{dt} \right), \quad (2.30a)$$

$$M_{ijkl}^{-1} = \lambda \delta_{ij} \delta_{kl} + \mu (\delta_{ik} \delta_{jl} + \delta_{il} \delta_{jk}), \quad (2.30b)$$

$$\frac{d\epsilon_{ij}^{\text{H}}}{dt} = \frac{1}{3} \delta_{ij} \frac{d}{dt} [f \theta^{\text{hr}} + (1 - f) C^{\text{H}} \bar{V}^{\text{M}} \theta^{\text{H}}], \quad (2.30c)$$

$$\frac{d\epsilon_{ij}^{\text{E}}}{dt} = \alpha \delta_{ij} \frac{dT}{dt}, \quad (2.30d)$$

where λ, μ are the Lamé constants of the metal; $\theta^{\text{hr}} = \epsilon_{kk}^{\text{T}}$ is hydride expansion, occurring during its precipitation and θ^{H} is the expansion of the metal lattice, when a mole of hydrogen corresponds to a mole of metal in solid solution. Note that, according to Peisl (1978), $\theta^{\text{H}} = \bar{V}^{\text{H}} / \bar{V}^{\text{M}}$. A relation similar to Eq. (2.30c) has been also used by Lufrano et al. (1996). Finally, α is the thermal expansion coefficient of the metal, which is assumed to be equal to that of the hydride.

2.5. De-cohesion model for crack growth

The idea of simulating fracture by considering cohesive tractions has been introduced by Dugdale (1960) and Barenblatt (1962). Ahead of a crack-tip there is a fracture process zone, where material deteriorates in a ductile (void growth and coalescence) and/or

brittle (hydride cleavage) mode. According to the de-cohesion model, the de-cohesion layer, which is a slice as thick as the fracture process zone, is taken off the material, along the crack path. Along the boundaries, created by the cut, the cohesive traction is applied. All information on the damage is contained in the distribution of the cohesive traction, which depends on de-cohesion layer boundary displacements. The shape of the traction–displacement function depends on the failure process. However, in the case of tensile separation, the most important features are the maximum cohesive traction, σ_{\max} , and the energy of de-cohesion, ϕ_0 :

$$\phi_0 = \int_0^{\delta_c} \sigma_n d\delta_n, \quad (2.31)$$

where σ_n is the normal cohesive traction and δ_n is the respective normal displacement, which equals the sum of the displacements on both sides of the de-cohesion layer. Also δ_c is the normal displacement, which corresponds to complete failure and consequently to zero normal cohesive traction. Details of the model for crack growth under plane strain conditions have been presented in previous publications (e.g. Varias, 1998b; Varias and Massih, 2000b). The model has been used for the solution of several fracture problems (e.g. Needleman, 1987; Varias et al., 1990; Tvergaard and Hutchinson, 1992).

In the present study, cohesive traction is assumed to vary according to the following relation:

$$\sigma_n = \begin{cases} E_i \frac{\delta_n}{\delta_0}, & \delta_n \leq \delta_l \\ \sigma_{\max}, & \delta_l \leq \delta_n \leq \delta_f \\ \sigma_{\max} - E_f \frac{\delta_n - \delta_f}{\delta_0}, & \delta_f \leq \delta_n \leq \delta_c \\ 0, & \delta_c \leq \delta_n, \end{cases} \quad (2.32)$$

where δ_0 is a constant length of the order of hydride thickness ($\delta_0 = 1 \mu\text{m}$); E_i and E_f are the de-cohesion moduli, which are assumed to be constant; δ_l is the normal displacement at initiation of damage, at which maximum cohesive traction is reached. Unloading starts, when normal displacement exceeds δ_f . Note that δ_f depends on σ_{\max} and ϕ_0 according to the following relation:

$$\delta_f = \left[\phi_0 + \frac{1}{2} \sigma_{\max}^2 \delta_0 \left(\frac{1}{E_i} - \frac{1}{E_f} \right) \right] \sigma_{\max}^{-1}. \quad (2.33)$$

The relations for the energy of de-cohesion and the maximum cohesive traction as well as their derivation, based on experimental measurements, are discussed in the following. As shown by Rice (1968), the energy of de-cohesion, related to a cohesive zone ahead of a crack-tip, in an elastic material, is equal to the critical value of J -integral, when fracture is imminent:

$$\phi_0 = J_c = \frac{1 - \nu^2}{E} K_{Ic}^2. \quad (2.34)$$

J_c and K_{Ic} are the critical values of J -integral and stress intensity factor under plane strain conditions, respectively. Also E and ν are Young's modulus and Poisson's ratio

of the material. Consequently, the de-cohesion energy is the energy required per unit crack advance. Ahead of the crack, the material is a composite made of brittle hydride and relatively tough metal. Therefore, the fracture toughness of the material, expressed by the energy of de-cohesion, depends on hydride volume fraction, f , along the crack plane. A mixture rule has been assumed to provide the energy of de-cohesion of the composite material:

$$\phi_0 = f\phi_0^{\text{hr}} + (1 - f)\phi_0^{\text{M}}. \quad (2.35)$$

ϕ_0^{M} is the de-cohesion energy of the material, when there is no hydride along the crack plane over a distance from the crack-tip $X \gg \delta_0$; i.e. $f = 0$, along the crack plane over the distance X . Therefore, ϕ_0^{M} is related to the critical stress intensity factor of the metal, K_{I}^{M} , by a relation similar to Eq. (2.34). It has been assumed that hydrogen in solid solution does not affect the fracture toughness of the metal. Any hydrogen effect on the toughness of the solid solution is easily incorporated, by changing ϕ_0^{M} in Eq. (2.35).

In Eq. (2.35), ϕ_0^{hr} is the energy of de-cohesion, when there is only hydride along the crack plane over a distance from the crack-tip $X \gg \delta_0$; i.e. $f = 1$, along the crack plane over the distance X . Note that the hydride is surrounded by metal. According to previous studies (e.g. Shi and Puls, 1994; Wäppling et al., 1998), the geometry of a long hydride, along the crack plane, corresponds to the threshold stress intensity factor for delayed hydride cracking. Therefore, ϕ_0^{hr} is related to the threshold stress intensity factor for delayed hydride cracking, K_{I}^{hr} , by a relation similar to Eq. (2.34). Note that the experimental values of the threshold stress intensity factor include both the energy required for the generation of the new surface, due to crack growth, as well as any plastic dissipation in the metal matrix, which surrounds the crack-tip hydride. Consequently, if K_{I}^{hr} is set equal to the experimentally derived threshold stress intensity factor, as in the present study, the plastic dissipation near the crack-tip is also taken into account.

When crack growth is imminent or during crack growth, the material is damaged over a distance from the crack-tip of the order of the characteristic length, associated with the failure process. At the beginning of the damage zone, at the current crack-tip, material is completely damaged and it does not sustain any traction. At the end of the damage zone, away from the crack-tip, material damage initiates and therefore the maximum cohesive traction is sustained (e.g. Varias and Massih, 2000b). The metal can sustain different maximum cohesive traction from that of the hydride. Therefore, the maximum cohesive traction of the composite material along the crack plane, depends on the hydride volume fraction. In the present analysis, the maximum cohesive traction is given by the following relation:

$$\sigma_{\text{max}} = \sqrt{f\sigma_{\text{hr}}^2 + (1 - f)\sigma_{\text{M}}^2}, \quad (2.36)$$

which is derived by assuming that the part of de-cohesion energy during loading satisfies a relation similar to Eq. (2.35). In Eq. (2.36), σ_{M} is the maximum cohesive traction, sustained by the material, when crack growth is imminent or during crack growth and when there is no hydride along the crack plane over a distance from the

crack-tip $X \gg \delta_0$. According to theoretical studies for the crack-tip field in elastic plastic materials (e.g. Hutchinson, 1968; Rice and Johnson, 1970; Drugan et al., 1982), the maximum hoop stress, along the crack plane, is nearly equal to 3 times the yield stress of the material. Therefore, the maximum cohesive traction, σ_M , which is equal to the maximum hoop stress along the crack plane, when crack growth is imminent or during crack growth, is taken equal to 3 times the yield stress of the metal, $\sigma_M = 3\sigma_0$. Based on this assumption, it will be shown that the maximum hydrostatic stress near the crack-tip is calculated with adequate accuracy. Note that, in the present study, the metal has been assumed to be linear elastic in the bulk of the body. However, in deriving the de-cohesion constitutive relations, the elastic–plastic behavior of the metal has been considered in order to accurately predict the strong effect of hydrostatic stress on hydrogen diffusion.

In relation (2.36), σ_{hr} denotes the maximum cohesive traction, sustained by the material, when crack growth is imminent or during crack growth and when there is only hydride along the crack plane over a distance from the crack-tip $X \gg \delta_0$. δ -hydride is a brittle phase. It is assumed that a brittle phase fractures, when a critical principal stress is applied, which is equal to the fracture strength of the phase. Consequently, σ_{hr} is assumed to be equal to hydride fracture strength.

Relations (2.35) and (2.36) provide the average properties of the de-cohesion layer over its thickness, which is of the order of $1 \mu\text{m}$.

Consider a particle of the de-cohesion layer ahead of a crack-tip. Due to hydrogen diffusion and hydride formation, hydride volume fraction changes locally with time. Consequently, the de-cohesion properties at the particle, under consideration, change with time. Maximum cohesive traction is reached, when δ_n corresponds to a normal traction, satisfying relation (2.36). As time increases, de-cohesion energy continues to change according to relation (2.35). Unloading starts, when relation (2.33) is satisfied. It is assumed that de-cohesion energy does not change during unloading. The part of the de-cohesion energy, during unloading, is minimized by choosing the largest value of E_f , for which quasi-static unloading exists (see Appendix A in Varias et al., 1990).

The finite element implementation of the hydride-induced embrittlement model is presented in Appendix B. In the following, the numerical simulation of the initiation of delayed hydride cracking in Zircaloy-2 is discussed.

3. Simulation of hydride-induced embrittlement and fracture in Zircaloy-2

The mathematical model for hydrogen embrittlement in hydride forming metals, presented in Section 2, is valid for a pure metal/hydrogen system, where brittle hydrides may precipitate and be accommodated elastically.

Zirconium alloys, such as Zircaloy-2, which are used in the core of nuclear reactors, have a very small concentration of additional elements (e.g. Northwood and Kosasih, 1983), which do not affect the processes of hydrogen diffusion and hydride precipitation. Zircaloy-2 is a single phase α -alloy. Then, the hydride-induced embrittlement model can be applied by considering the mechanical, thermal, hydrogen-diffusion and hydride-precipitation properties of the alloy.

Table 1

Material properties used in the finite element calculations. The material properties correspond to Zircaloy-2 and δ -hydride ($\text{ZrH}_{1.66}$). The source of information is included

E, ν	80.4 GPa, 0.369	Wäppling et al. (1998)
E_i, E_f	80.4, 1.5 GPa	Assumption
σ_{hr}	580 MPa	Wäppling et al. (1998); Shi and Puls (1994)
σ_{Zr}	1740 MPa	Wäppling et al. (1998)
K_{I}^{Zr}	$30 + 0.045(T - 300)$ MPa $\sqrt{\text{m}}$	Huang (1993); Wäppling et al. (1998)
K_{I}^{hr}	$3.22 + 0.02205(T - 300)$ MPa $\sqrt{\text{m}}$	Wäppling et al. (1998)
δ_0	1 μm	Assumption
D^{H}	$2.17 \times 10^{-7} \exp(-35087.06/RT)$ m^2/s	Sawatzky (1960)
Q^{H}	25122 J/mol	Sawatzky (1960)
C^{TS}	$6.3741 \times 10^5 \exp(-34542.75/RT)$ mol/ m^3	Kearns (1967)
$C^{\text{H,hr}}$	1.02×10^5 mol/ m^3	Calculation
\bar{V}^{H}	7×10^{-7} m^3/mol	Dutton et al. (1977)
\bar{V}^{Zr}	14.0×10^{-6} m^3/mol	Calculation
\bar{V}^{hr}	16.3×10^{-6} m^3/mol	Puls (1984)
θ^{hr}	0.1636	Calculation based on Puls (1984)
θ^{H}	0.05	Calculation based on Peisl (1978)
x	1.66	δ -hydride (ZrH_x) (e.g. Puls, 1984)
ρ	6490 kg/ m^3	Pure zirconium density
$\Delta \bar{H}^{\text{hr}}$	-63517.41 J/mol	Calculation based on the experimental terminal solid solubility of hydrogen
k	$9.37683 + 0.0118T$ W/mK	Hagrman et al. (MATPRO version 11)
c_p	$226.69 + 0.206639T - 6.4925 \times 10^{-5} T^2$ J/kg K	Hagrman et al. (MATPRO version 11)
α	5.96×10^{-6} K^{-1}	Average value based on Hagrman et al. (MATPRO version 11)

The consideration of elastic behavior in the bulk of the body and consequently of elastic hydride accommodation leads to re-dissolution of the crack-tip hydrides, after the fracture of the hydrides and the reduction of the hydrostatic stress level. Such a behavior has been observed in electron-microscopy studies of vanadium (Takano and Suzuki, 1974). In the case of zirconium alloys, the metal matrix yields during hydride precipitation. As a consequence, the crack-tip hydrides are more stable and may re-dissolve only partially after fracture. For this reason, the present model is used only for the simulation of one complete cycle of hydride precipitation and fracture at crack growth initiation.

The numerical simulation of hydride-induced embrittlement in Zircaloy-2 has been stimulated by crack growth observations in irradiated fuel cladding rods, during experiments, which were conducted by ABB Atom. The material properties, used in the present simulations, are given in Table 1 together with the source of information. Note that σ_{hr} is based on estimates, given by Shi and Puls (1994), which related hydride fracture strength to Young's modulus, E , of the material. σ_{Zr} is taken equal to 3 times the irradiated Zircaloy-2 yield stress. The threshold stress intensity factor for delayed

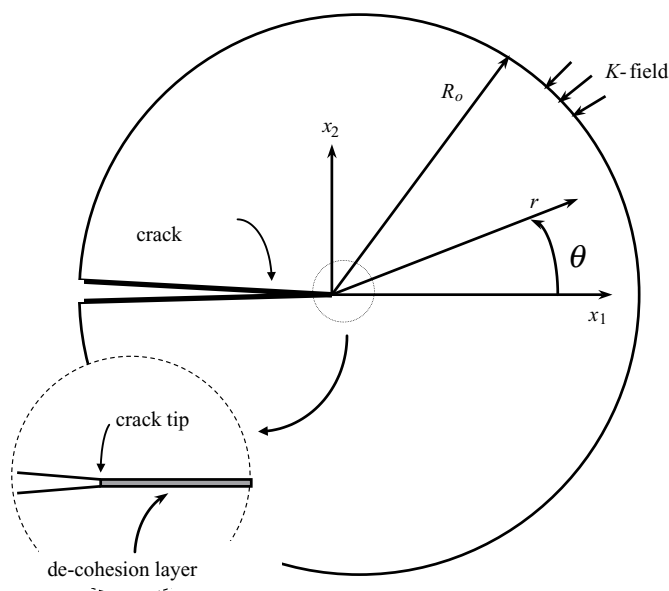


Fig. 1. The boundary value problem, which is considered for the simulation of delayed hydride cracking, under K-field dominance. The hydrogen flux on the crack face, the crack line and the remote circular boundary, where mode-I K-field is applied, is taken equal to zero. $T = 300^\circ\text{C}$, $C^{\text{HT}}(t=0) = 6438.5 \text{ mol/m}^3$. Due to symmetry conditions with respect to the crack line, only half of the space needs to be analyzed. Cohesive traction is applied along the crack plane.

hydride cracking, K_{I}^{hr} , as well as the critical stress intensity factor for Zircaloy-2, K_{I}^{Zr} , have also been obtained from experimental measurements of irradiated material.

3.1. Delayed hydride cracking under K-field dominance

3.1.1. Boundary value problem

A semi-infinite crack is considered in a homogeneous material (Fig. 1). Cartesian (x_1, x_2) and polar (r, θ) coordinates are used. The origin of the coordinate system is the initial crack-tip position. x_2 -axis is normal to the crack plane and θ is measured from the crack line on the (x_1, x_2) plane. The geometry shows no variation along the normal to the (x_1, x_2) plane.

The mode-I K-field dominates away from the crack-tip:

$$\sigma_{ij} = \frac{K_{\text{I}}}{\sqrt{2\pi r}} f_{ij}(\theta), \quad r \gg L_{\text{hr}}. \quad (3.1)$$

K_{I} is the mode-I stress intensity factor and f_{ij} is the respective well-known angular stress distribution (e.g. Rice, 1968). L_{hr} is the size of the area, where hydrides are expected to precipitate and fracture ahead of the crack-tip. L_{hr} is of the order of $10 \mu\text{m}$ (e.g. Simpson and Nuttall, 1977; Efsing and Pettersson, 2000). K-dominance is accomplished by applying the tractions, derived by Eq. (3.1), on a semi-circular

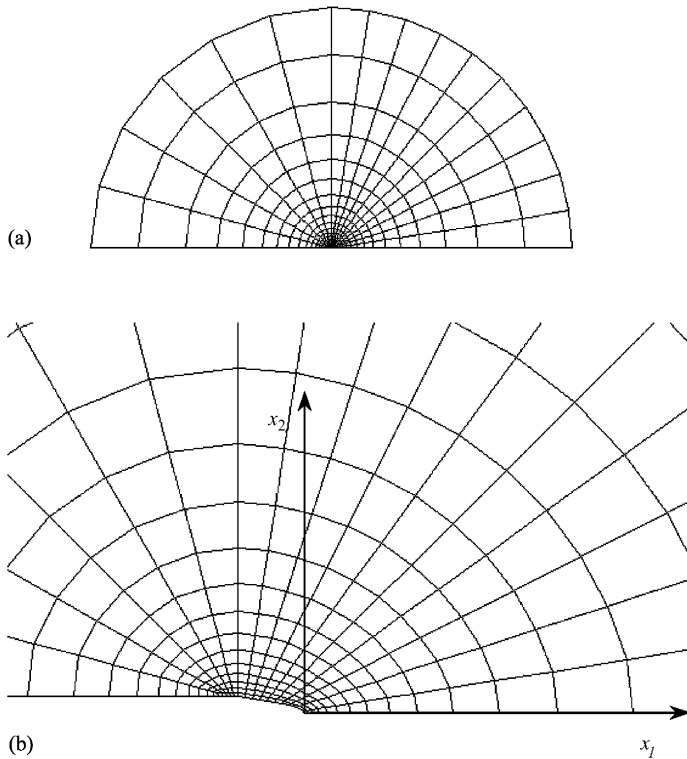


Fig. 2. Finite element mesh. (a) Remote region. Traction are applied along the semi-circular boundary, derived from the mode-I K-field. Zero hydrogen flux is prescribed along the crack line, the crack face and the semi-circular boundary. (b) Near-tip region.

boundary of radius $R_0 = 0.1$ m; only half of the space is considered, due to symmetry with respect to the crack line (Fig. 2a). Along the crack plane cohesive traction is applied, according to relation (2.32). Plane strain conditions prevail.

The stress intensity factor initially increases at a rate equal to $0.2 \text{ MPa}\sqrt{\text{m}} \text{ s}^{-1}$ for 100 s and subsequently remains constant at the maximum value of $20 \text{ MPa}\sqrt{\text{m}}$. The maximum stress intensity factor corresponds to the second stage of delayed hydride cracking, during which the crack growth velocity is independent or weakly dependent on K_I , according to experimental data (e.g. Efsing and Pettersson, 1996, 2000; Huang and Mills, 1991). The initial stress intensity factor rate has been taken about equal to that expected during the loading of a cracked fuel cladding (Varias and Massih, 2000a), according to previous studies on fuel pellet/cladding mechanical interaction (Massih et al., 1995).

The temperature of the material is constant, with respect to time and space, equal to 300°C . Initial total hydrogen concentration is homogenous and equal to 6438.5 mol/m^3 ($\approx 1000\text{ppm}$). Note that 300°C is in the range of temperatures, which develop in the nuclear fuel cladding of boiling water reactors, during operation (e.g. Forsberg and

Massih, 1990). Efsing and Pettersson (1996, 2000) have also considered the same temperature and initial hydrogen concentration, mentioned previously, in their Zircaloy-2 experiments.

The material is assumed to be insulated by a zirconium oxide layer and consequently zero hydrogen flux is prescribed along the crack face and the remote semi-circular boundary. Due to symmetry conditions, hydrogen flux is also taken equal to zero along the crack line. It has been already mentioned that the size of the near-tip area, which is rich in hydrides, is of the order of $10\text{ }\mu\text{m}$. Consequently one may conclude, that during the precipitation and fracture of the near-tip hydrides, the hydrogen concentration far from the crack-tip at the remote boundary ($R_0 = 0.1\text{ m}$) will change negligibly. Therefore, the consideration of zero hydrogen flux on the remote semi-circular boundary does not have any significant effect on the simulation.

The finite element mesh, used in the calculations is presented in Fig. 2. Seven hundred and ninety nine quadrilaterals, made of four cross triangles, have been used. The first member of the triangular element family is considered, with three nodes at the vertices and linear interpolation functions.

Fig. 2b shows the details of the crack-tip. An elliptical crack-tip profile has been considered. The initial crack-tip opening, given by the maximum initial distance between the crack faces, is equal to $1\text{ }\mu\text{m}$, i.e. of the order of the thickness of the hydrides, which are expected to precipitate. The initial crack-tip opening has been considered in order to approach the crack-tip blunting conditions, which are expected before the precipitation and fracture of the near-tip hydrides.

3.1.2. Hydride precipitation and fracture ahead of the crack-tip

Experimental studies show that the embrittlement and fracture of hydride forming metals is characterized by repeated hydride precipitation and cleavage ahead of the growing crack (Takano and Suzuki, 1974; Grossbeck and Birnbaum, 1977; Simpson and Nuttall, 1977). According to Simpson and Nuttall, in the case of zirconium alloys the crack-tip blunts before the cleavage of the near-tip hydrides; i.e. the hydrides form at a small distance away from the crack-tip. Indeed, their electron microscope fractographs reveal the presence of striations and plate-like regions on the fracture surface. The striations are produced by void growth and coalescence of thin ligaments parallel to the crack front. The plate-like regions between the striations are produced by hydride cleavage. The interstriation spacing, ranges from 6 to $50\text{ }\mu\text{m}$ in the temperature range of 150 – 325°C and reveals the size of the near-tip area, which is rich in hydrides, precipitating during delayed hydride cracking. These results have been derived from experiments on Zr–2.5Nb alloys. Similar studies have been performed by Efsing and Pettersson (2000) for irradiated Zircaloy-2. According to Efsing and Pettersson a plate-like region is produced by the fracture of several hydrides of length 1 – $10\text{ }\mu\text{m}$, rather than a single hydride.

The simulation of crack growth initiation due to the above embrittlement process is discussed in the following. The progress of hydride precipitation with time is presented in Fig. 3. The hydride volume fraction distribution along the crack line is shown immediately after the completion of load application, i.e. at 100 s , as well as after 1 , 4 and 4.36 days. A region with relatively large hydride volume fraction develops ahead

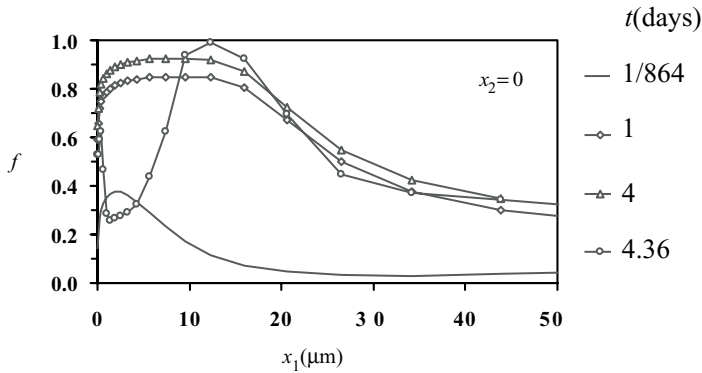


Fig. 3. Hydride volume fraction distribution along the crack line, as time progresses.

of the crack-tip. At $t=4$ days, hydride volume fraction, f , is greater or equal to 0.90 within the range of $2.5 \mu\text{m} \leq x_1 \leq 12.4 \mu\text{m}$. Therefore, the peak value of f is away from the crack-tip. The development of the area ahead of the crack-tip, which is rich in hydride volume fraction, can be interpreted as the precipitation of near-tip hydrides. The size of this area, where $f \geq 0.9$, is about equal to $10 \mu\text{m}$. Note that the predicted size of the near-tip hydride area is larger or equal to the hydride platelet length observed by Efsing and Pettersson (2000). It is also of the same order of magnitude as that of the interstriation spacing, observed in the experiments of Simpson and Nuttall.

The hydride volume fraction distribution, corresponding to 4.36 days in Fig. 3, is quite different. The hydride volume fraction is relatively small ahead of the crack-tip over a distance of the order of $10 \mu\text{m}$. A new hydride volume fraction peak develops further away. Also there is a small region of about half a micron at the crack-tip, where f is larger than 0.5. This redistribution of hydride volume fraction has been produced within about 100 s and it is attributed to the fracture of the near-tip hydrides and the associated decrease of the near-tip hydrostatic stress. Thus a microcrack has been generated ahead of the main crack tip, leaving behind a thin ligament with $0.5 < f < 0.65$. Failure of this ligament is expected to occur in a ductile mode, due to the relatively small hydride volume fraction. Therefore, the present numerical simulation is in agreement with the development of striations during delayed hydride cracking. However, consideration of matrix plastic deformation would result into reduction of hydrogen re-dissolution due to the additionally required plastic work.

The distribution of the stress trace is presented in Fig. 4 along the crack line for the same time instants as those considered in Fig. 3. Note that immediately after the application of the remote loading, at $t=100$ s, when the hydride volume fraction is relatively small in the near-tip region, the maximum stress trace is equal to $7.17\sigma_0$. The maximum stress trace is in agreement with the slip line solution ahead of a stationary crack (Hutchinson, 1968). The distributions, which correspond to 1 and 4 days, show that the stress trace is significantly smaller due to hydride precipitation. The stress trace distributions, for $t=1$ and 4 days, are also relatively flat, corresponding to a small hydrogen flux due to stress gradient, thus explaining the small increase of the

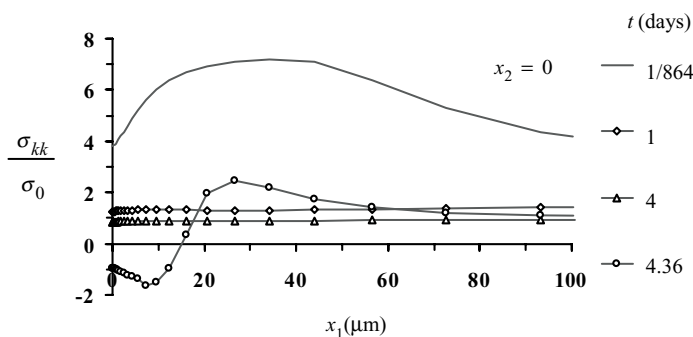


Fig. 4. Normalized stress trace distribution along the crack line, as time progresses.

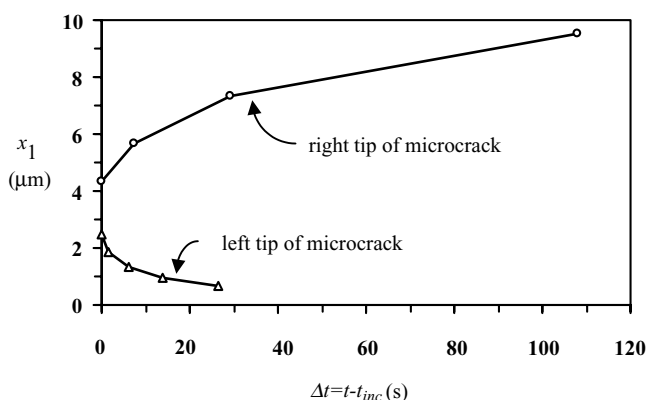


Fig. 5. Positions of left and right tips of the generated microcrack vs. elapsed time, $\Delta t = t - t_{inc}$. $t_{inc}(=4.36$ days) is the incubation period for the generation of the microcrack.

hydride volume fraction within the elapsed time of 3 days. Hydride fracture, at $t = 4.36$ days, results into stress redistribution. The hoop stress on the crack plane is zero along the microcrack faces and about $1.25\sigma_0$ in the area of the ligament. However, the stress trace, along the de-cohesion layer boundaries, becomes negative due to the expansion, which corresponds to the remaining hydride volume fraction. Note that $f(t=0)=0.06$. Although under compression, the hydrides in this area do not completely dissolve, due the large hydride volume fraction, before fracture; the hydrides are expected to continue dissolving with time.

The generated microcrack propagates fast on both directions. Fig. 5 shows the positions of the left and right tips of the microcrack with time. Incubation time, t_{inc} , is the time required for the generation of the first microcrack of the order of hydride thickness. In the present study, the incubation time is taken equal to the time required for the release of the first node and satisfies the above definition, due to the density of the grid. Note that consideration of a larger initial microcrack would not affect the calculation

of the incubation time, due to the fast microcrack propagation. According to the calculations, t_{inc} is equal to 4.36 days. Also, according to Fig. 5, the microcrack propagates 8.88 μm , within the time period of 107.8 s, at an average speed of 8.24×10^{-8} m/s. Note that the microcrack average speed does not correspond to the crack growth rate of stage II delayed hydride cracking, since we have simulated only the first cycle of the crack growth process. Note also that the different deformation fields of a growing and a non-growing crack in an elastic–plastic material may affect the distribution of hydrogen. Consequently, these different fields may imply different crack growth rates at initiation and after substantial crack growth. However, it is expected that a variation of the average microcrack speed, due to different material parameters, corresponds to a similar variation of the stage II crack growth rate.

The above calculations have been performed for K_{I}^{hr} equal to 9.24 $\text{MPa}\sqrt{\text{m}}$, which is an experimentally derived threshold stress intensity factor for delayed hydride cracking of irradiated Zircaloy-2. Note that the above value of K_{I}^{hr} is significantly larger than that which is predicted by linear elastic fracture mechanics models. For example, according to a cohesive zone model (Varias and Massih, 2000b), $K_{\text{I}}^{\text{hr}} = \sigma_{\text{hr}} \sqrt{Ah\pi/2}$, where h is hydride thickness and Ah is the length of the cohesive zone (i.e. the damage zone within the near-tip hydride). A increases with temperature and may take values from 1 to 5, when temperature range is 350–550 K. Consequently, according to the above cohesive zone model, $K_{\text{I}}^{\text{hr}} = 1.63 \text{ MPa}\sqrt{\text{m}}$ at 300°C, assuming that $A = 5$. The difference is attributed to (i) the plastic dissipation of the matrix during hydride formation and fracture and (ii) the actual orientation of the near-tip hydrides, which depends on the orientation of the hydride habit planes. Indeed, according to the experimental data of Huang and Mills (1991), the threshold stress intensity factor for delayed hydride cracking decreases when the density of the hydride habit planes in the crack plane increases. According to the same experimental data, material texture affects also stage II crack growth rates. The higher the density of hydride habit planes in the crack plane the higher the crack growth rate is. Therefore, by varying K_{I}^{hr} in the present model, texture effects could be implicitly taken into account. Indeed, crack growth calculations with $K_{\text{I}}^{\text{hr}} = 1.63 \text{ MPa}\sqrt{\text{m}}$ show that the average microcrack speed is doubled.

According to delayed hydride cracking experiments by Efsing and Pettersson (1996) at 300°C, 1000 ppm initial hydrogen concentration and 9.5 $\text{MPa}\sqrt{\text{m}}$ threshold stress intensity factor, the stage II crack growth rate is 6.2×10^{-8} m/s. However, the material is unirradiated Zircaloy-2, with significantly smaller yield stress ($\sigma_0 = 230 \text{ MPa}$). Huang and Mills (1991) have also measured stage II crack growth rates in the range 10^{-8} – 5×10^{-8} m/s. Their experiments were also performed with unirradiated Zircaloy-2 and the variation on crack growth rate was attributed to the texture of the material. Huang and Mills also tested irradiated material at 149°C and 204°C and measured a 50-fold increase in the crack growth rates. Recent experimental measurements by Efsing and Pettersson (2000) on irradiated Zircaloy-2 also provided larger stage II crack growth rates. At 300°C and initial hydrogen concentration between 560 and 1900 ppm, Efsing and Pettersson measured crack growth rates equal to 9.5×10^{-7} m/s.

The incubation period measured by Efsing and Pettersson (1996) at 300°C varied between 18 and 30 h. However, before testing, the specimens were subjected to a thermal cycle in order to promote crack growth. Initially the specimens were kept for 4 h

at 360°C. Subsequently, the temperature was reduced to 300°C and the loading was applied. The irradiated Zircaloy-2 experiments (Efsing and Pettersson, 2000) provided incubation periods within 16–24 h; in these tests thermal cycles were also applied before the loading. According to Simpson and Puls (1979), when specimens are cooled to the test temperature the relatively small hydrides that form and grow during this excursion are more susceptible to dissolution, due to high elastic constraint, and this enhances the driving force for hydrogen diffusion into the crack-tip process zone. Such an argument is in agreement with the size effect on the accommodation of a misfitting spherical precipitate, discussed by Lee et al. (1980). Note that, in the present simulation, the initial hydrogen concentration is assumed to be uniform, associated with an unconstrained material expansion, which does not lead to the development of residual stresses. The above mentioned temperature effect on crack growth could be introduced by considering a non-uniform initial hydrogen concentration which should be also associated with an initial non-zero and non-uniform stress distribution. However, it is beyond the scope of the present study.

3.2. Hydride precipitation and fracture in a plate under tensile loading and temperature gradient

3.2.1. Boundary value problem

The present boundary value problem has been designed in order to estimate the effect of surface cracks on hydrogen embrittlement and fracture in the cladding of light water reactor fuel rods. The most critical case corresponds to a crack along the rod axis. During reactor operation, the rod is subjected to external pressure by coolant water, internal pressure by helium gas and fission products, as well as to stresses, caused by fuel pellet-cladding mechanical interaction (Massih et al., 1995). Note that the pellet-cladding mechanical interaction is the major source of loading and may lead to the development of significant tensile hoop stresses. The expansion of zirconium oxide on the waterside of the cladding may also produce tensile hoop stresses. On the external rod surface, the oxidation of zirconium by coolant water leads to the generation of hydrogen, which subsequently diffuses in the cladding. The heat, which is generated in the fuel pellet, is transferred through the cladding to the water. The heat transfer process leads to the development of temperature gradients in the fuel cladding, with significant effects on hydrogen distribution (Forsberg and Massih, 1990).

The development of external axial cracks has been observed in experiments, conducted by ABB Atom. These cracks are generated by the fracture of the brittle external oxide layer and most often do not exceed one tenth of the cladding thickness. However, if the oxide layer is removed, for example in places where the rod is in contact with other structural components, a layer of a continuous hydride network can develop, due to hydrogen thermal transport. The hydride network is very brittle and may lead to the development of cracks of depth up to a quarter of the cladding thickness. The present study examines the possibility of advance of the above cracks by delayed hydride cracking, during reactor operation. Note that cracks can also develop on the inner side of a cladding tube, due to stress corrosion cracking caused by iodine and/or caesium, which are produced during nuclear fission. However, this mechanism

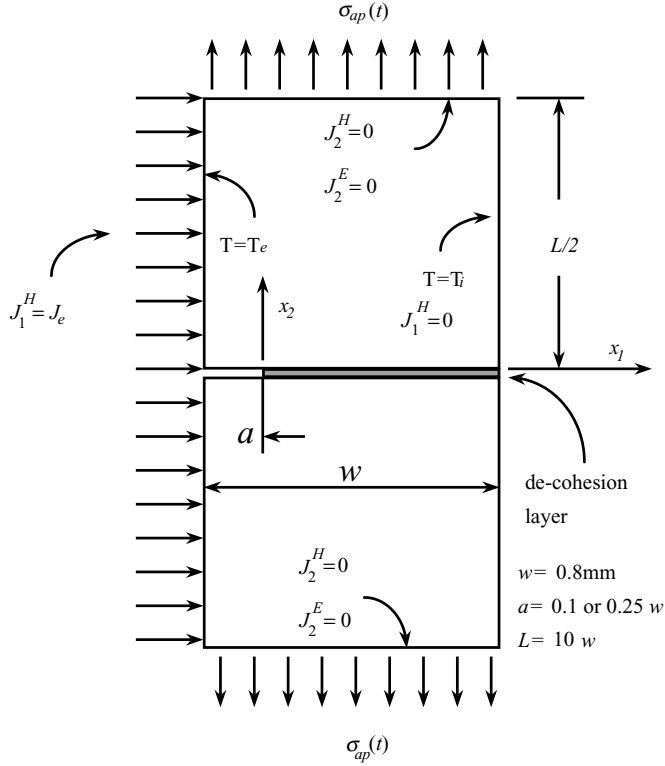


Fig. 6. Boundary value problem for the simulation of hydrogen embrittlement of a Zircaloy-2 cracked plate under tension and temperature gradient. Due to symmetry with respect to x_1 -axis, only the upper half of the plate has been analyzed. Cohesive traction is applied along the crack plane.

is not under consideration. The development and fracture of radial hydrides, under pellet-cladding mechanical interaction, could also be responsible for the generation of cracks on the inner cladding surface at temperatures below $\sim 320^\circ\text{C}$. Indeed delayed hydride cracking is difficult to initiate above $\sim 320^\circ\text{C}$ (e.g. Efsing and Pettersson, 2000; Shi and Puls, 1994). In the present boundary value problem the inner surface temperature exceeds 320°C .

The geometry has been approximated by a cracked plate. Note that this approximation is good for small cracks and initial damage growth. In the present problem the crack length is either $1/67$ or $1/27$ of the cladding tube inner radius, which is equal to 5.325 mm . Also the difference between the temperature distributions in the cladding cylinder, under consideration, and a plate of the same thickness, both subjected to the same surface temperatures, is negligible. The boundary value problem is shown in Fig. 6. A Cartesian coordinate system is considered with origin at the initial crack-tip position. x_1 -axis is normal to the crack front and lies on the crack plane. The geometry does not show any variation along the normal to the (x_1, x_2) -plane. Note that the letter w is used for plate thickness in Fig. 6 as well as throughout Section 3.2.

The plate thickness is taken to be equal to the actual cladding wall thickness (in this case $w = 0.8$ mm). A long planar surface crack, of depth a ($= 0.1w$ or $0.25w$), has been considered on one side. A remote tensile stress, σ_{ap} , is applied normal to the crack faces. The stress builds up gradually at a rate of 10 MPa/s, according to previous studies for pellet-cladding mechanical interaction (Massih et al., 1995). The remote stress is considered to be constant after the maximum value of 500 MPa is reached. The maximum stress is below the yielding stress of the fuel cladding.

The oxidation process is assumed to produce a constant inflow of hydrogen on the crack-side surface of the plate, which is equal to 0.122×10^{-7} mol/(m² s) (Forsberg and Massih, 1990). The same inflow of hydrogen is also assumed to occur on the crack faces. A zero hydrogen flux is considered on the other side of the plate, where stress and temperature gradients do not allow hydrogen outflow. Symmetry conditions require also zero hydrogen flux on the crack plane as well as on the remote plane, where σ_{ap} is applied.

The temperature on both plate surfaces is constant, being equal to 567 K, on the crack side, and 607 K, on the other side. The initial temperature distribution is assumed to be linear across the thickness of the plate. These internal and external surface temperatures are expected during reactor operation, according to previous studies on hydrogen and temperature distribution in fuel cladding (Forsberg and Massih, 1990). Symmetry conditions require that the heat flux on the crack plane as well as on the remote plane, where σ_{ap} is applied, is zero. In the present application, the heat-conduction term in relation (2.19) is dominant.

The initial distribution of the hydrogen concentration is assumed to be uniform. Calculations have been performed for $C^{HT}(t=0) = 2500, 6438.5, 9657.7$ and $20\,000$ mol/m³, which are about equal to 388, 1000, 1500 and 3200 ppm, respectively. Note that a hydrogen concentration equal to 388 ppm corresponds to 1900 days of reactor operation (Forsberg and Massih, 1990). Also 3200 ppm is about equal to the average hydrogen concentration measured in some places where part of the oxide layer was lost; the average concentration was calculated through the cladding wall thickness. The uniform material expansion due to the initial hydrogen concentration is assumed to be unconstrained and therefore no residual stresses are considered at $t=0$.

Due to symmetry with respect to the crack plane only half of the plate has been analyzed, under plane strain conditions. Along the crack plane, cohesive traction is applied, in order to simulate material damage and crack growth.

Fig. 7 shows the finite element mesh in the case of $a = 0.1w$. Six hundred and seventy seven quadrilaterals, made of four cross triangles, have been used. The near-tip region of the finite element mesh and the coordinate system is shown in Fig. 7a. The initial crack-tip opening is equal to 1 μm , i.e. of the order of hydride thickness. A similar mesh with 765 quadrilaterals has been used in the case of $a = 0.25w$.

3.2.2. Material degradation under conditions leading to loss of K-field dominance

The following discussion is mainly for the case, where $a = 0.1w$ and the initial hydrogen concentration is 2500 mol/m³ (≈ 388 ppm). However, the conclusions, derived from this case, are also valid for larger cracks ($a \leq 0.25w$) as well as for larger values of initial hydrogen concentration ($C^{HT}(t=0) \leq 1500$ ppm). Indeed, the results,

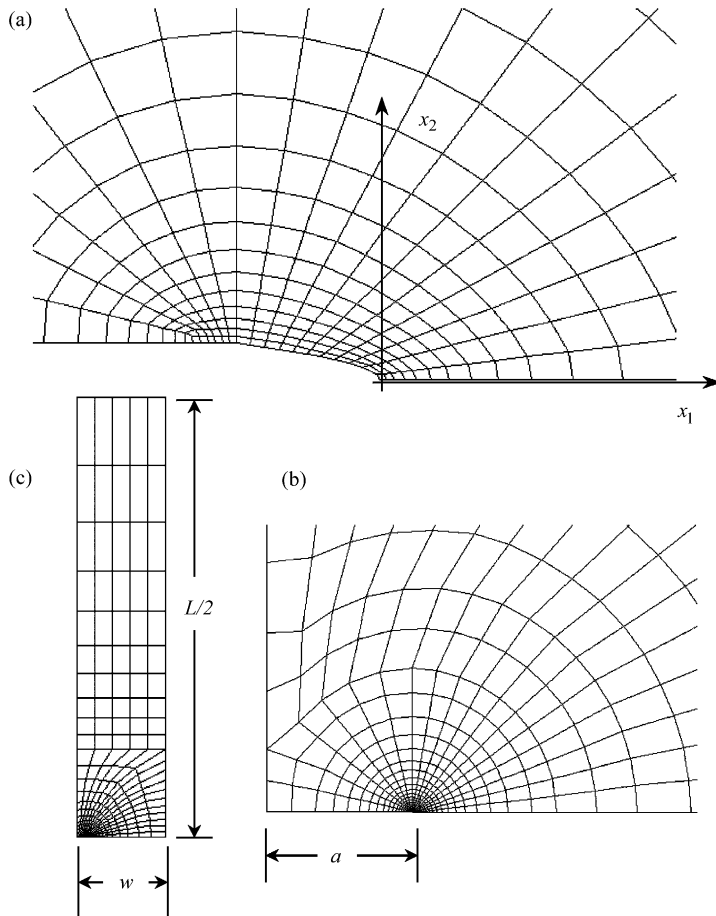


Fig. 7. Finite element mesh, used in the cracked plate problem. (a) Part of the mesh near the crack-tip. (b) Part of the mesh, containing the crack on the left side of the plate. (c) The complete mesh for the upper half of the plate, needed to be analyzed.

for $a = 0.25w$ and $C^{\text{HT}}(t=0) = 388, 1000, 1500$, and 3200 ppm, which are briefly discussed at the end of this section, support the conclusions derived from the main case.

Within the period of load application, $0 \leq t \leq 50$ s, hydrogen diffuses towards the crack-tip under the influence of the gradients of stress, temperature and hydrogen concentration in the solid solution. According to a preliminary study (Varias and Massih, 1999, 2000a), the effect of stress and concentration gradients is dominant near the crack-tip, over a distance of the order of $10 \mu\text{m}$. Further away the contribution of temperature gradient becomes important. Note that, due to the energy flow boundary conditions and the geometry, the temperature gradient is nearly constant. Consequently, the contribution of temperature gradient to hydrogen flux depends weakly on x_1 -coordinate.

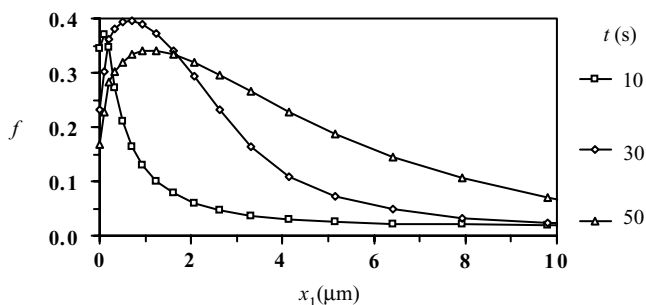


Fig. 8. Hydride volume fraction distribution along the crack plane, during the application of remote loading ($t \leq 50$ s).

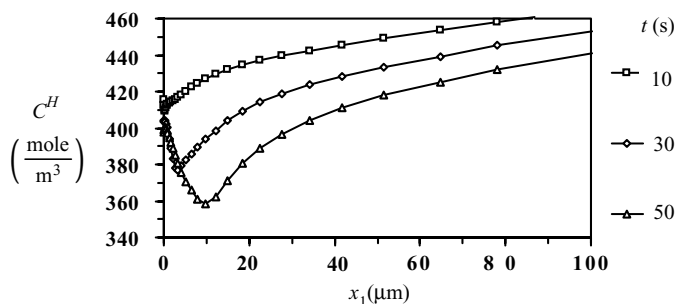


Fig. 9. Distribution of hydrogen concentration in solid solution along the crack plane, during the application of remote loading ($t \leq 50$ s).

The distribution of hydride volume fraction, f , along the crack plane, is presented in Fig. 8 for the period of load application. Near-tip hydrides start precipitating. The distribution of hydrogen concentration in solid solution, C^H , along the crack plane and during load application, is presented in Fig. 9. Note that, over the distance, which is presented in Fig. 9, hydride volume fraction is not zero and consequently the hydrogen concentration in solid solution is equal to the terminal solid solubility, C^{TS} . Hydrogen concentration in solid solution decreases with time, away from the crack-tip, at a distance of 10 μm or larger. Also at a given time (e.g. $t = 50$ s), C^H and consequently C^{TS} decrease, as the crack-tip is approached, and reach a minimum value, at a distance from the crack-tip, which depends on time. The variations of C^H with time as well as along the crack plane are attributed to the effect of hydrostatic stress on hydrogen terminal solid solubility. Indeed, according to relation (2.29), increase of hydrostatic stress leads to decrease of terminal solid solubility, due to the interaction of the applied stress with the expansion of a hydride.

Fig. 10 presents the distribution of normalized hydrostatic stress along the crack plane, during the period of load application. Note that, very close to the crack-tip, hydrostatic stress decreases due to hydride precipitation and the associated expansion.

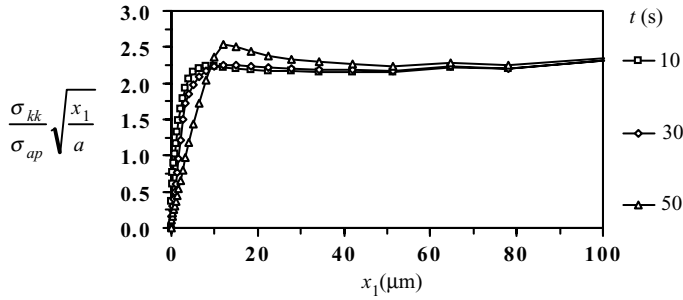


Fig. 10. Normalized hydrostatic stress distribution along the crack plane, during the application of remote loading ($t \leq 50$ s). K-field is dominant in the range of $30 \leq x_1 \leq 80 \mu\text{m}$.

Away from the crack-tip, over the range $30 \leq x_1 \leq 80 \mu\text{m}$, all curves collapse to one at a normalized stress level equal to about 2.2. This is the annulus where K-field dominates. Indeed, when the near-tip stress distribution is in agreement with the well-known square-root singularity of the K-field, the following relation is valid, along the crack plane:

$$\frac{\sigma_{kk}}{\sigma_{ap}} \sqrt{\frac{x_1}{a}} = \frac{\sqrt{2}(1+\nu)K_I}{\sigma_{ap}\sqrt{\pi a}} = \text{const.} \quad (3.2)$$

According to relation (3.2), the stress intensity factor of the dominating K-field, at the end of loading, is about equal to $9 \text{ MPa}\sqrt{\text{m}}$. This value is slightly smaller than the threshold stress intensity factor for delayed hydride cracking, which is equal to $9.2 \text{ MPa}\sqrt{\text{m}}$ at 570 K, according to the relation of Table 1. Note that the variation of the experimental values of the threshold stress intensity factor can be significant due to material texture (e.g. 20% as in Huang and Mills, 1991). Consequently, based on the above value of the applied stress intensity factor and the variation of experimental threshold data, one may not conclude on the initiation or not of the crack growth by delayed hydride cracking.

The variation of hydride volume fraction distribution, along the crack plane, within the period of the first 8 h, is presented in Fig. 11. The near-tip hydride precipitation continues within the period of 4 h. Subsequently, partial hydride dissolution occurs and the hydride volume fraction decreases. This is attributed to hydrogen thermal transport, which is dominant, away from the crack-tip. Indeed, the hydrogen diffuses to the low temperature side of the plate and creates a layer relatively rich in hydride volume fraction (e.g. Sawatzky, 1960; Varias and Massih, 2000a). This layer is under compressive hydrostatic stress, due to hydride expansion. On the other hand, tensile hydrostatic stresses develop on the hot side of the plate. The redistribution of the hydrogen, away from the crack-tip, affects the near-tip field; the near-tip hydrostatic stress decreases significantly, leading to partial dissolution of the near-tip hydrides. Note that a smaller amount of hydride re-dissolution is expected if elastic–plastic material behavior and hydride accommodation is taken into account.

The significant decrease of hydrostatic stress near the crack-tip is verified in Fig. 12a, where the distributions of hydrostatic stress along the crack line at 50 s and

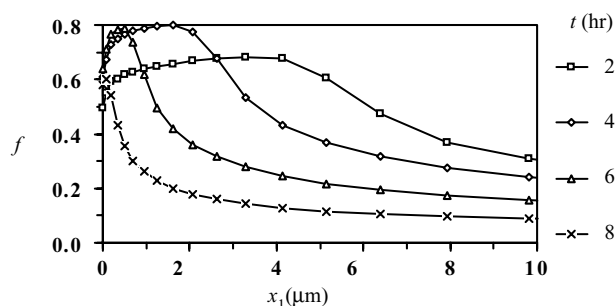
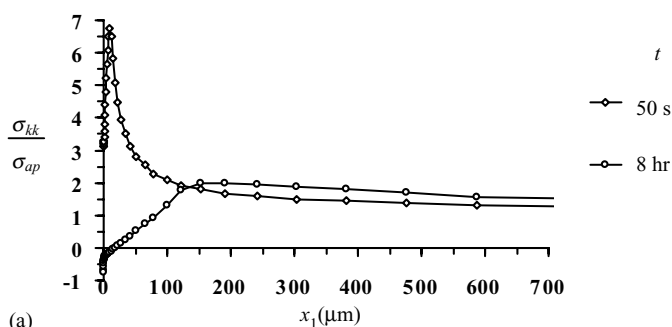
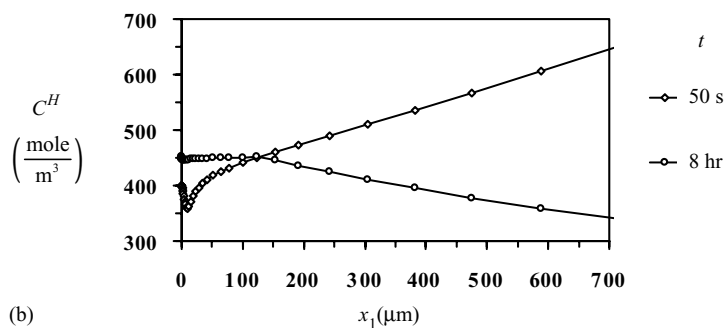


Fig. 11. Hydride volume fraction distribution along the crack plane, during the first 8 h after the application of remote loading.



(a)



(b)

Fig. 12. Comparison of field quantity distributions, along the crack plane, at completion of load application, ($t = 50$ s), and after several hours, ($t = 8$ h). (a) Stress trace, σ_{kk} , normalized by remotely applied tensile stress. (b) Hydrogen concentration in solid solution.

8 h are presented. Note that K-field dominance is lost. Consequently, linear elastic fracture mechanics is no longer applicable for the appreciation of the integrity conditions of the plate. The respective distributions of hydrogen concentration in solid solution are also presented in Fig. 12b. The significant reduction of hydrogen concentration in the hot side of the plate was caused by thermal transport.

Fig. 13a shows the distribution of hydride volume fraction along the crack plane, within a period of 5 days; the applied tensile stress is constant at 500 MPa. The hydride volume fraction increases again and approaches steady-state conditions. The distributions of hydrogen concentration in the solid solution and normalized stress trace confirm the approach to steady-state conditions. These distributions are presented in Figs. 13b and c for the period of 5 days. Indeed the total hydrogen flux along the crack plane is negligibly small for $x_1 > 4 \mu\text{m}$ (see Figs. 14a and b). Away from the crack-tip, in the range of $x_1 > 80 \mu\text{m}$, the effect of stress gradient on hydrogen flux is negligible. In the same range, the effects of temperature and hydrogen concentration gradients are opposite, resulting into nearly zero total hydrogen flux. Near the crack-tip, in the range of $4 < x_1 < 40 \mu\text{m}$, the effect of hydrogen concentration gradient on hydrogen flux is negligible, as expected from the nearly constant hydrogen concentration in the solid solution (see Fig. 13b). In this range the stress and temperature gradient contributions to hydrogen flux are nearly opposite.

According to Fig. 13a, the hydride volume fraction does not exceed 0.7 and decreases significantly within a distance of $2 \mu\text{m}$ from the crack-tip. Consequently, severe material embrittlement is limited to a very small area near the crack-tip. Therefore, no crack growth is expected under the applied loading. Indeed, the de-cohesion model showed no unloading along the crack plane. Calculations were also performed for a gradual reduction of the surface temperatures and the applied stress over a period of several hours, in order to provide preliminary results of reactor shut down effect on hydride precipitation, ahead of the hypothetical crack (Varias, 1999a). Again no crack growth was predicted.

When the crack length is equal to a quarter of the cladding thickness ($a = 0.25w$), the applied stress intensity factor exceeds the experimentally measured threshold value, at the end of load application. Indeed, the normalized hydrostatic stress level (see relation (3.2)) is about equal to 2.5 and the applied stress intensity factor is about $16 \text{ MPa}\sqrt{\text{m}}$, at $t = 50 \text{ s}$. However, the numerical simulation shows no crack growth. K-field dominance is lost shortly after the application of remote loading, due to hydrogen thermal transport. After the loss of K-field dominance, the near-tip region is under relatively low hydrostatic stress, which does not favor the near-tip hydride precipitation.

All calculations, mentioned previously, have been performed for an average Zircaloy-2 fracture toughness (Wäppling et al., 1998), given in Table 1, which was derived from the experimental measurements of Huang (1993). The actual experimental data show scatter and therefore smaller values of Zircaloy-2 fracture toughness are possible. For this reason, additional calculations have been performed for a Zircaloy-2 toughness, which is by 25% smaller than the value given in Table 1; the selection of the new value of the fracture toughness is in agreement with the scatter in the experimental data. The crack length for all additional calculations was taken equal to $0.25w$. Three cases of initial hydrogen concentration were considered: 1000, 1500 and 3200 ppm. Crack growth initiation was only predicted for the extreme case of 3200 ppm; details on hydride precipitation and microcrack propagation are given by Varias and Massih (2001). The extreme hydrogen concentration was actually observed in places of the fuel cladding, where the oxide layer was partially lost due to spalling, during service. In this case, according to experiments, crack growth may occur.

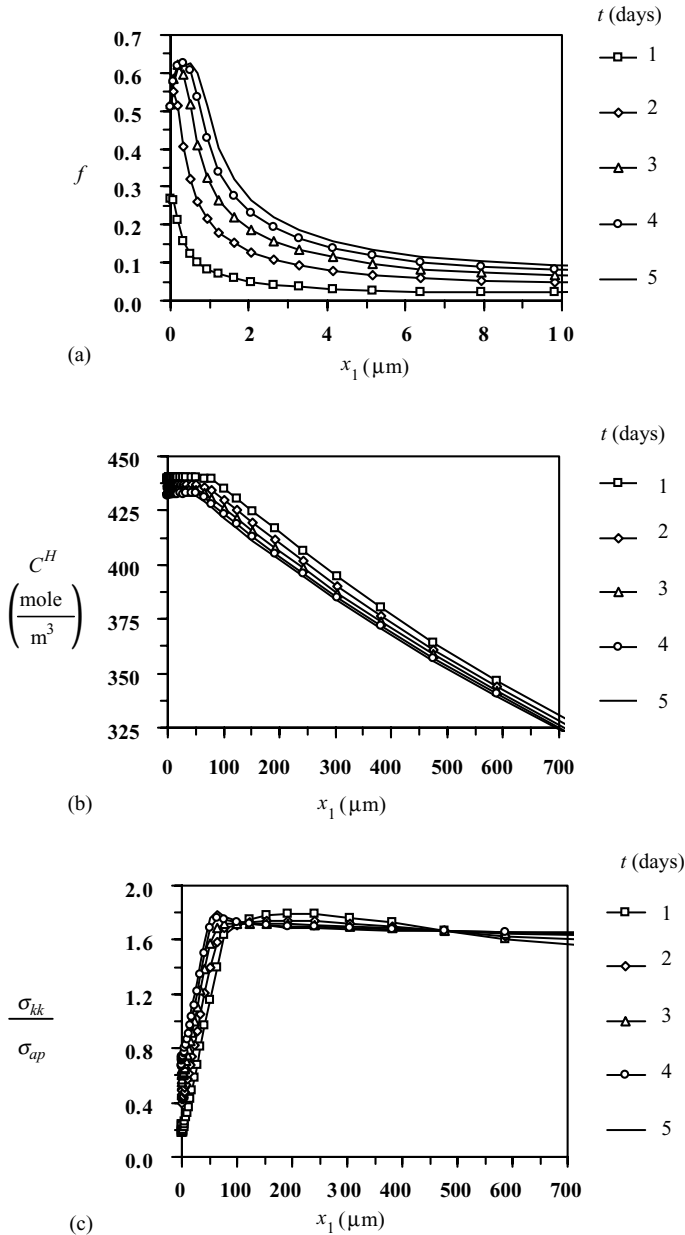


Fig. 13. Approach of steady-state conditions after 5 days under constant remote tensile stress. (a) Hydride volume fraction distribution along the crack plane. (b) Distribution of hydrogen concentration in solid solution along the crack plane. (c) Distribution of normalized stress trace along the crack plane.

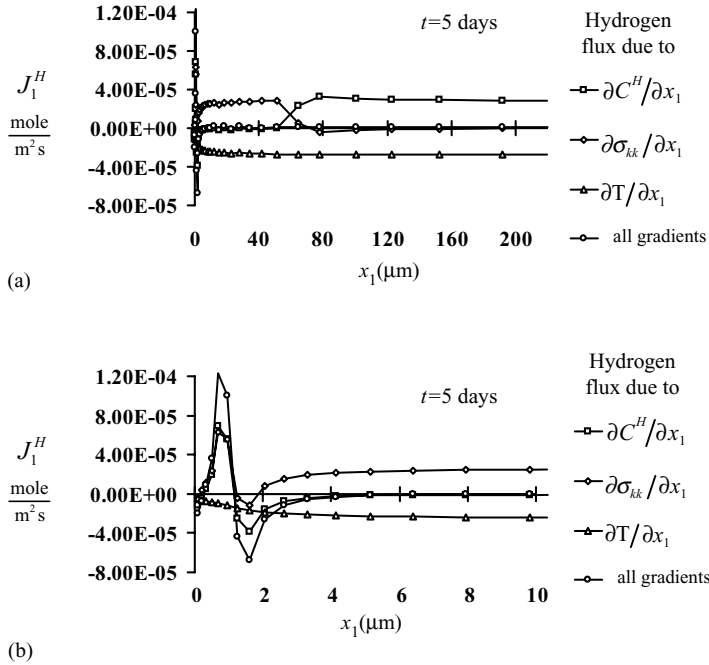


Fig. 14. Hydrogen flux distribution along the crack plane, (a) away from the crack-tip, and (b) near the crack-tip. Total hydrogen flux is negligible for $x_1 > 4 \mu\text{m}$.

The present study shows the importance of considering the coupling of the operating physical processes, when simulating hydride-induced embrittlement. Such consideration is expected to improve the calculations on structural integrity.

4. Concluding remarks

A mathematical model for the simulation of hydride-induced embrittlement and fracture of metals has been developed. The model takes into account the coupling of the operating physical processes, namely: (i) hydrogen diffusion, (ii) hydride precipitation, (iii) non-mechanical energy flow and (iv) hydride/solid-solution deformation. Material damage and crack growth are also simulated by using de-cohesion model.

The hydrogen embrittlement model has been implemented numerically into a finite element framework and tested successfully against experimental data and analytical solutions on hydrogen thermal transport (Varias and Massih, 1999, 2000a).

The model has been used for the simulation of Zircaloy-2 hydrogen embrittlement and initiation of delayed hydride cracking under conditions encountered in the fuel cladding of light water reactors, during operation. The numerical simulation predicts hydride precipitation at a small distance from the crack-tip. When the remote loading is sufficient, the area, which is rich in hydride volume fraction, fractures. Thus a

microcrack is generated, leaving behind a ductile ligament, in agreement with experimental observations.

The above model has been developed for a pure metal/hydrogen system, where brittle hydrides may precipitate and be accommodated elastically. Hydrogen diffusion in the hydride has been neglected for being significantly slower than the diffusion in the solid solution. It has been also assumed that hydrogen does not affect the elastic moduli of the metal. Finally, the elastic and thermal properties of the hydride and the solid solution were taken to be identical in the development of the governing equations.

The model can be extended to single or multi-phase alloys without any changes, if the additional elements have a very small concentration and do not affect the operating processes. Then, the properties of the alloy with respect to elastic deformation, energy flow, hydrogen diffusion and hydride precipitation should be used. This is the case of Zircaloy-2. It is, however, possible that due to alloying and thermal treatment different phases are produced, which have different hydrogen diffusion characteristics. Such an example is α - β titanium alloys. At room temperature, hydrogen transport in β -phase titanium is several orders of magnitude more rapid than in α -phase titanium. This results in different hydrogen embrittlement behaviors, which depend on the microstructure of the alloy (e.g. Nelson et al., 1972). In this case the present model should be appropriately modified.

The consideration of elastic behavior in the bulk of the body and consequently of elastic hydride accommodation leads to re-dissolution of the crack-tip hydrides, after the fracture of the hydrides and the reduction of the hydrostatic stress level. Such a behavior has been observed in electron-microscopy studies of vanadium (Takano and Suzuki, 1974). In the case of zirconium alloys, the metal matrix yields during hydride precipitation. As a consequence, the crack-tip hydrides are more stable and may re-dissolve only partially after fracture. For this reason, the present model is used only for the simulation of one complete cycle of hydride precipitation and fracture at crack growth initiation. An extension of the present model, which would take into account elastic-plastic hydride accommodation (Lufrano et al., 1998), is indeed useful, for simulations beyond crack growth initiation as well as for consideration of all parameters, which play a role in constraint effects (Varias and Massih, 2000b). The difference between the hydrogen solvus temperatures, derived by cooling and heating experiments, is also taken into account with the elastic-plastic hydride accommodation (Birnbaum et al., 1976).

Another direction for further development of the present model is the consideration of different mechanical and thermal properties of the solid solution and the hydride. In this case, the approaches, which are used in composite materials (e.g. Christensen, 1979), could be adopted for developing the governing equations. Along this direction is also the consideration of the effect of hydrogen on the elastic moduli of the solid solution, if this is indeed important (Senkov et al., 1996). This effect has also implications on hydrogen chemical potential in the solid solution (Li et al., 1966) and therefore on hydrogen terminal solid solubility.

In the present version of the model simple mixture rules (relations (2.35) and (2.36)) have been used for the derivation of the energy of de-cohesion and the maximum cohesive traction. However, the maximum hydrostatic stress, which is expected ahead

of the crack-tip in an elastic–plastic material before the precipitation of near-tip hydrides, is recovered. Consequently, the strong effect of hydrostatic stress distribution on hydrogen diffusion and hydride precipitation near the crack-tip has been taken into account with adequate accuracy. Note that, if perfect cohesion is considered, a hydride precipitates at the tip and no ductile ligament is formed during fracture (Varias and Massih, 2000a). Therefore, the de-cohesion model improves the performance of the hydrogen embrittlement model, which is based on elastic behavior of the bulk of the material. The de-cohesion model takes also into account the time variation of energy of de-cohesion, due to the time-dependent process of hydride precipitation.

The improvements, discussed above, require precise measurements of hydride properties.

Acknowledgements

A.G. Varias acknowledges the support of ABB Atom AB under the contracts 4500026874 and 4500028097. Financial support for the study on hydride-induced embrittlement in metals is currently provided by the Foundation for Knowledge and Competence Development (Project Grant Hög 2000, KK-Stiftelsen, Sweden).

Appendix A. Thermodynamic forces driving hydrogen diffusion and non-mechanical energy flow

Denbigh (1951) presents a derivation of the thermodynamic forces for diffusion and flow of energy. In the following this derivation is extended to the metal–hydride system under consideration.

Continuum thermodynamics, based on a caloric equation of state, assumes that the local internal energy per unit mass, u , is determined by the thermodynamic state, specified by n thermodynamic sub-state variables, v_1, v_2, \dots, v_n , and the specific entropy, s (e.g. Truesdell and Toupin, 1960). The sub-state variables could be strains and concentrations of substances. In the present study, the material under consideration is made of hydrogen and metal in solid solution as well as metal hydride, MH_x . Then, the strains, ε_{ij} , and the concentrations of hydrogen, C^{Hy} , and metal, C^M , being in solid solution, as well as the concentration of hydride, C^{hr} , can be chosen as sub-state variables. Note that the above three local concentrations are given in moles per unit total volume, occupied by all phases. Therefore, $C^{Hy} = (1 - f)C^H$ and $C^{hr} = fC^{H,hr}/x$, where C^H , $C^{H,hr}$ and f are defined in Section 2.1.

The variation of specific internal energy for a material particle is given by the relation:

$$du = T ds + \tau_i dv_i. \quad (A.1)$$

The thermodynamic tensions, τ_i , associated with the strains and the concentrations of the various components are related to the actual stresses and the chemical potentials of the components, respectively. When the mechanical work is fully recoverable, as in the

present study, which is based on elastic material deformation, the external stress power for a material particle is equal to the rate of the work of the thermodynamic tensions, associated with the strains. Then, for a particle of the material under consideration, the internal energy variation is

$$\rho \, du = \rho T \, ds + \sigma_{ij} \, d\epsilon_{ij} + \mu^H \, dC^{Hy} + \mu^M \, dC^M + \mu^{hr} \, dC^{hr}. \quad (A.2)$$

Hydride precipitation is assumed to occur under equilibrium conditions:

$$\mu^{hr} = \mu^M + x\mu^H. \quad (A.3)$$

The total mass of the metal in the solid solution and the hydride is constant. Consequently, $dC^M = -dC^{hr}$, which leads to the following simplification:

$$\begin{aligned} \mu^H \, dC^{Hy} + \mu^M \, dC^M + \mu^{hr} \, dC^{hr} \\ = \mu^H (dC^{Hy} + x \, dC^{hr}) + (\mu^{hr} - \mu^M - x\mu^H) \, dC^{hr} = \mu^H \, dC^{HT}, \end{aligned} \quad (A.4)$$

where C^{HT} is the total hydrogen concentration in the solid solution and the hydride. By substituting Eq. (A.4) into Eq. (A.2), one derives the rate of internal energy for a particle of the material:

$$\rho \frac{du}{dt} = \rho T \frac{ds}{dt} + \sigma_{ij} \frac{d\epsilon_{ij}}{dt} + \mu^H \frac{dC^{HT}}{dt}. \quad (A.5)$$

Note that the term $\mu^H \, dC^{HT}$ is integrable. Therefore, under chemical equilibrium, the free energy function of the metal–hydride system exists.

According to Section 2, the conservation of energy and hydrogen mass, is expressed by the following differential equations:

$$\rho \frac{du}{dt} = \sigma_{ij} \frac{d\epsilon_{ij}}{dt} - \frac{\partial J_k^E}{\partial x_k}, \quad (A.6)$$

$$\frac{dC^{HT}}{dt} = - \frac{\partial J_k^H}{\partial x_k}. \quad (A.7)$$

Substitution of Eqs. (A.6) and (A.7) into Eq. (A.5), leads to the following expression, after some algebraic manipulations:

$$\rho \frac{ds}{dt} + \frac{\partial}{\partial x_k} \left(\frac{J_k^E - \mu^H J_k^H}{T} \right) = - \frac{J_m^E}{T^2} \frac{\partial T}{\partial x_m} - J_n^H \frac{\partial}{\partial x_n} \left(\frac{\mu^H}{T} \right). \quad (A.8)$$

Let us define:

$$\psi = - \frac{J_k^E}{T^2} \frac{\partial T}{\partial x_k} - J_m^H \frac{\partial}{\partial x_m} \left(\frac{\mu^H}{T} \right), \quad (A.9a)$$

$$S_k = \frac{J_k^E - \mu^H J_k^H}{T}, \quad (A.9b)$$

integrate over a volume V and apply Gauss's divergence theorem. Then Eq. (A.8) leads to the following relation on entropy variation over a volume V :

$$\frac{d}{dt} \int_V \rho s \, dV + \int_S S_k n_k \, dS = \int_V \psi \, dV. \quad (A.10)$$

S is the boundary of the volume V and n_k the respective normal vector, pointing outwards. The first term of the left-hand side provides the rate of entropy in the specified volume. The second term of the left-hand side represents the rate of outflow of entropy, or in other words the rate of entropy due to heat and hydrogen flux on the bounding surface; note that the entropy of a mole of hydrogen flowing through the bounding surface is equal to Q^H/T . Consequently, the term of the right-hand side is the rate of internal generation of entropy due to hydrogen diffusion and non-mechanical energy flow in the volume, under consideration. Therefore ψ , defined in Eq. (A.9a), is the rate of internal generation of entropy per unit volume. Note that hydride precipitation, occurring under chemical equilibrium, does not contribute to the internal generation of entropy. Subsequently, one may combine relations (A.9a) and (2.3) and derive the thermodynamic forces for the non-mechanical energy flow and the diffusion of hydrogen, given by Eq. (2.2).

Appendix B. Finite element implementation of the hydride-induced embrittlement model

The finite element implementation of the constitutive relations for the deformation and de-cohesion problem has been discussed in previous papers (e.g. Varias and Massih, 2000b). The implementation is based on the principle of virtual work. In the following, a discussion is presented for the finite element implementation of the governing equations (2.7) and (2.19) for hydrogen diffusion and non-mechanical energy flow, respectively.

The following initial and boundary conditions supplement the governing equations:

$$C^{HT} = C_0^H \quad \text{at } t = 0, \quad (\text{B.1a})$$

$$T = T_0 \quad \text{at } t = 0, \quad (\text{B.1b})$$

$$C^{HT} = C_b^H \quad \text{on } S_b, \quad (\text{B.1c})$$

$$J_k^H n_k = \varphi^H \quad \text{on } S_\varphi, \quad (\text{B.1d})$$

$$T = T_s \quad \text{on } S_T, \quad (\text{B.1e})$$

$$-k \frac{\partial T}{\partial x_i} n_i = \varphi^E \quad \text{on } S_F, \quad (\text{B.1f})$$

where C_0^H and T_0 are the initial hydrogen concentration and temperature, which may vary within material volume V . If C_0^H is larger than hydrogen terminal solid solubility, the initial hydrogen concentration in the solid solution equals the terminal solid solubility and the initial hydride volume fraction is calculated, according to Eq. (2.8). A

similar comment is valid for C_b^H , which is the prescribed hydrogen concentration on S_b , a part of the bounding surface S . Note that, for the calculation of C^{TS} , stress and temperature distributions have to be taken into account. φ^H is the prescribed hydrogen flux on S_φ and T_s is the prescribed temperature on S_T . Also φ^E is the prescribed heat flux on S_F . Note that $S_b \cup S_\varphi = S$ and $S_T \cup S_F = S$. The quantities C_b^H , φ^H , T_s and φ^E may vary with time.

The finite element equations are derived from variational descriptions of diffusion and energy flow. For this purpose variations of hydrogen concentration, δC^H , and temperature, δT , are considered, which satisfy the boundary conditions. Therefore:

$$\delta C^H = 0 \quad \text{on } S_b, \quad (\text{B.2a})$$

$$\delta T = 0 \quad \text{on } S_T. \quad (\text{B.2b})$$

Relation (2.7) is multiplied by a hydrogen concentration variation, satisfying Eq. (B.2a). Subsequently, it is integrated over the volume V . After some elaboration the following expression is derived, which is valid at any time t :

$$\begin{aligned} \int_V \delta C^H \frac{dC^{HT}}{dt} dV = & - \int_{S_\varphi} \delta C^H \varphi^H dS - \int_V (1-f) D^H \frac{\partial C^H}{\partial x_k} \frac{\partial (\delta C^H)}{\partial x_k} dV \\ & - \int_V (1-f) \left(-\frac{D^H \bar{V}^H}{3RT} \frac{\partial \sigma_{mm}}{\partial x_k} + \frac{D^H Q^H}{RT^2} \frac{\partial T}{\partial x_k} \right) C^H \frac{\partial (\delta C^H)}{\partial x_k} dV. \end{aligned} \quad (\text{B.3})$$

The above relation is simplified if, within a time increment Δt , the change of hydride volume fraction is included in C^H . Δt is of the order of a characteristic time, introduced by diffusion and hydride size, or smaller. Then:

$$\frac{dC^{HT}}{dt} = (1-f_t) \frac{dC^H}{dt}. \quad (\text{B.4})$$

Note that C^H is no longer the hydrogen concentration in solid solution but the hydrogen concentration in a part of the material, which at time t is in the form of solid solution and has volume $(1-f_t)V$. Within the time interval Δt , during which Eq. (B.4) is applied, that part of the material may change from solid solution to hydride/solid-solution composite. In the present calculations the change in total hydrogen concentration is not allowed to exceed $1.5 \times 10^{-4} C^{H,hr}$, within the time increment. Relation (B.4) has been also used by Lufrano et al. (1996) in their derivation of the differential equation for hydrogen mass balance.

Spatial discretization is obtained by introducing the usual finite element interpolation for hydrogen concentration, hydride volume fraction, temperature and stress trace. For example hydrogen concentration is calculated from nodal values, as follows:

$$C^H = a_q C_q^H, \quad (\text{B.5})$$

where a_q and C_q^H are the interpolation function and the nodal hydrogen concentration value for node- q , respectively.

Substitution of relation (B.4) into Eq. (B.3) and use of spatial discretization leads to the finite element equations for hydrogen diffusion:

$$C_{pq} \frac{dC_q^H}{dt} + (D_{pq}^1 + D_{pq}^2) C_q^H = F_p, \quad (\text{B.6a})$$

$$C_{pq} = \int_V (1 - f_t) a_p a_q dV, \quad (\text{B.6b})$$

$$D_{pq}^1 = \int_V (1 - f_t) D^H \frac{\partial a_p}{\partial x_k} \frac{\partial a_q}{\partial x_k} dV, \quad (\text{B.6c})$$

$$D_{pq}^2 = \int_V (1 - f_t) \left(-\frac{D^H \bar{V}^H}{3RT} \frac{\partial a_r}{\partial x_k} \sigma_{mm}^r + \frac{D^H Q^H}{RT^2} \frac{\partial a_s}{\partial x_k} T_s \right) a_q \frac{\partial a_p}{\partial x_k} dV, \quad (\text{B.6d})$$

$$F_p = - \int_{S_p} a_p \varphi^H dS. \quad (\text{B.6e})$$

The time derivative of hydrogen concentration is approximated by

$$\frac{dC_q^{H,t+\Delta t}}{dt} = \frac{1}{\Delta t} (C_q^{H,t+\Delta t} - C_q^{H,t}). \quad (\text{B.7})$$

Relation (B.6) is taken at time $t + \Delta t$, Eq. (B.7) is substituted into Eq. (B.6) and the D_{pq}^2 -term is transferred to the right-hand side, leading to the following relation (similar to the one developed by Sofronis and McMeeking (1989), for hydrogen diffusion due to concentration and stress gradients):

$$\left(\frac{1}{\Delta t} C_{pq} + D_{pq}^1 \right) C_q^{H,t+\Delta t} = F_p - D_{pq}^2 C_q^{H,t} + \frac{1}{\Delta t} C_{pq} C_q^{H,t}. \quad (\text{B.8})$$

Note that, by incorporating D_{pq}^2 -term in the right-hand side vector, the global stiffness matrix of the finite element equation becomes symmetric, which reduces the size of the problem and the time required for its solution.

The matrices C_{pq} , D_{pq}^1 and D_{pq}^2 are calculated by using the known nodal values of hydride volume fraction, temperature and stress from the previous calculation step. The value of hydride volume fraction corresponds to time t . However, the values of temperature and stress correspond to time $t + \Delta t$, according to the discussion at the end of this section. Vector F_p is calculated from the boundary conditions at time $t + \Delta t$. Note that the solution of relation (B.8) provides a preliminary hydrogen concentration value, $C_{t+\Delta t}^{H,pr}$, which according to Eq. (B.4) may include hydrogen in hydride. However this preliminary value can be used for the determination of the total hydrogen concentration:

$$C_{t+\Delta t}^{HT} = f_t C^{H,hr} + (1 - f_t) C_{t+\Delta t}^{H,pr}, \quad (\text{B.9})$$

as well as the new hydride volume fraction, $f_{t+\Delta t}$:

$$f^{pr} = \frac{C_{t+\Delta t}^{HT} - C_{t+\Delta t}^{TS}}{C^{H,hr} - C_{t+\Delta t}^{TS}}, \quad (\text{B.10a})$$

$$f_{t+\Delta t} = \begin{cases} 0, & f^{pr} < 0, \\ f^{pr}, & 0 \leq f^{pr} \leq 1. \end{cases} \quad (\text{B.10b})$$

$C_{t+\Delta t}^{\text{TS}}$ is calculated, based on the results for temperature and stress from the previous calculation step.

The new hydrogen concentration in the solid solution is derived, based on Eq. (B.10b):

$$C_{t+\Delta t}^{\text{H}} = \begin{cases} C_{t+\Delta t}^{\text{H},pr}, & f^{pr} < 0, \\ C_{t+\Delta t}^{\text{TS}}, & 0 \leq f^{pr}. \end{cases} \quad (\text{B.11})$$

The finite element equations for the non-mechanical energy flow problem are derived next.

Relation (2.19) is multiplied by a temperature variation, satisfying Eq. (B.2b). Subsequently, it is integrated over the volume V and the following expression is derived, which is valid at any time t :

$$\begin{aligned} & \int_V \delta T \rho c_p \frac{dT}{dt} dV + \int_V \delta T \frac{\Delta \tilde{H}^{\text{hr}}}{\bar{V}^{\text{hr}}} \frac{df}{dt} dV \\ &= - \int_{S_F} \delta T \varphi^{\text{E}} dS - \int_V k \frac{\partial T}{\partial x_i} \frac{\partial(\delta T)}{\partial x_i} dV - \int_V \delta T J_n^{\text{H}} \frac{\partial \mu^{\text{H}}}{\partial x_n} dV. \end{aligned} \quad (\text{B.12})$$

As in hydrogen diffusion, spatial discretization is introduced and the following finite element equations are derived:

$$H_{qr} \frac{dT_r}{dt} + K_{qr} T_r = \Phi_q^1 + \Phi_q^2 - L_{qs} \frac{df_s}{dt}, \quad (\text{B.13a})$$

$$H_{qr} = \int_V \rho c_p a_q a_r dV, \quad (\text{B.13b})$$

$$K_{qr} = \int_V k \frac{\partial a_q}{\partial x_i} \frac{\partial a_r}{\partial x_i} dV, \quad (\text{B.13c})$$

$$\Phi_q^1 = - \int_{S_F} a_q \varphi^{\text{E}} dS, \quad (\text{B.13d})$$

$$\Phi_q^2 = - \int_V a_q J_n^{\text{H}} \frac{\partial \mu^{\text{H}}}{\partial x_n} dV, \quad (\text{B.13e})$$

$$L_{qs} = \int_V \frac{\Delta \tilde{H}^{\text{hr}}}{\bar{V}^{\text{hr}}} a_q a_s dV. \quad (\text{B.13f})$$

Assuming that temperature time-derivative is given by

$$\frac{dT_r^{t+\Delta t}}{dt} = \frac{T_r^{t+\Delta t} - T_r^t}{\Delta t} \quad (\text{B.14})$$

and following an approach similar to that for hydrogen diffusion, one may derive the following algebraic system from (B.13):

$$\left(\frac{H_{qr}}{\Delta t} + K_{qr} \right) T_r^{t+\Delta t} = \Phi_q^1 + \Phi_q^2 - L_{qs} \frac{df_s^t}{dt} + \frac{H_{qr}}{\Delta t} T_r^t. \quad (\text{B.15})$$

Φ_q^1 is calculated from the boundary conditions at time $t + \Delta t$. Also, for the estimation of Φ_q^2 , the nodal values of temperature, hydrogen concentration, hydride volume fraction and stress from the previous calculation step are used.

A complete calculation cycle is as follows. At time t all field quantities are known: $u_i^t, \varepsilon_{ij}^t, \sigma_{ij}^t, C_i^H, f_t, T_t, dC_i^H/dt, df_t/dt, dT_t/dt$, where u_i are the components of the displacement vector of a material particle. A time increment Δt is considered and the following calculation steps are performed:

- (i) Material deformation problem is solved first. The boundary conditions of the applied tractions and/or displacements are defined at time $t + \Delta t$. The isotropic expansion strain rate due to hydrogen dissolution, hydride formation and thermal expansion is calculated by using the values and time rates of hydrogen concentration, hydride volume fraction and temperature at time t . De-cohesion model properties are also derived from hydride volume fraction and temperature distribution, at time t . By performing calculation step (i), $u_i^{t+\Delta t}$, $\varepsilon_{ij}^{t+\Delta t}$ and $\sigma_{ij}^{t+\Delta t}$ are calculated.
- (ii) The energy flow problem is solved next. The boundary conditions of the applied surface temperature and/or heat flux are defined at time $t + \Delta t$. Φ_q^2 -term is calculated, based on the distributions of temperature, hydrogen concentration and hydride volume fraction, at time t , as well as on the distribution of stress, $\sigma_{ij}^{t+\Delta t}$, calculated within step (i). The hydride volume fraction rate, at time t , is used for the calculation of L_{qs} -term. By performing calculation step (ii), $T_{t+\Delta t}$ is calculated.
- (iii) The hydrogen diffusion problem is solved at the end. The boundary conditions of the applied surface hydrogen concentration and/or hydrogen flux are defined at time $t + \Delta t$. In all terms f_t is used. D_{pq}^2 -term is calculated, based on the values $\sigma_{ij}^{t+\Delta t}$ and $T_{t+\Delta t}$, derived within steps (i) and (ii), respectively. By performing calculation step (iii), $C_{t+\Delta t}^H$ and $f_{t+\Delta t}$ are calculated.

The time step is calculated automatically by the finite element program, based on three criteria:

- (a) the displacement increment of any point along the de-cohesion layer boundary is not allowed to exceed $10^{-3} \delta_0$,
- (b) the temperature increment anywhere in the body is not allowed to exceed 0.5 K, and
- (c) the total hydrogen concentration increment anywhere in the body is not allowed to exceed $1.5 \times 10^{-4} \text{ C}^{\text{H,hr}}$.

In addition, no time step larger than 5 s is allowed, even if all the above criteria are satisfied (e.g. when approaching steady-state conditions).

The material deformation problem is solved by assuming a constant value of Young's modulus. In the case of Zircaloy, which is considered in the paper, E depends on temperature. However, for a temperature change of 40 K, the error in the value of E does not exceed 2.9%. The error in the calculations is further minimized by considering the value of E for the temperature in the crack-tip region, where embrittlement and fracture processes operate. When the variation of temperature, either in space or in time, is significant, its effect, on elastic moduli, should be taken into account (e.g. Povirk et al., 1990).

The performance of the program has been tested, successfully, under uncoupled and coupled cases of hydrogen diffusion, energy flow and decohesion (Varias, 1999b).

References

- Barenblatt, G.I., 1962. Mathematical theory of equilibrium cracks in brittle fracture. *Advances in Applied Mechanics* 7, 55–129.
- Boley, B.A., Wiener, J.H., 1960. *Theory of Thermal Stresses*. Wiley, New York.
- Birbaum, H.K., Grossbeck, M.L., Amano, M., 1976. Hydride precipitation in Nb and some properties of NbH. *Journal of the Less-Common Metals* 49, 357–370.
- Coleman, C.E., Ambler, J.F.R., 1977. Susceptibility of zirconium alloys to delayed hydrogen cracking. In: Lowe Jr. A.L., Parry, G.W. (Eds.), *Zirconium in the Nuclear Industry*, ASTM STP 633, American Society for Testing and Materials, pp. 589–607.
- Coleman, C.E., Hardie, D., 1966. The hydrogen embrittlement of α -zirconium—a review. *Journal of Less-Common Metals* 11, 168–185.
- Christensen, R.M., 1979. *Mechanics of Composite Materials*. Wiley, New York.
- Denbigh, K.G., 1951. *The Thermodynamics of the Steady State*. Methuen, London.
- Drugan, W.J., Rice, J.R., Sham, T.-L., 1982. Asymptotic analysis of growing plane strain tensile cracks in elastic-ideally plastic solids. *Journal of the Mechanics and Physics of Solids* 30, 447–473.
- Dugdale, D.S., 1960. Yielding of steel sheets containing slits. *Journal of the Mechanics and Physics of Solids* 8, 100–108.
- Dutton, R., Nuttall, K., Puls, M.P., Simpson, L.A., 1977. Mechanisms of hydrogen induced delayed cracking in hydride forming materials. *Metallurgical Transactions A* 8A, 1553–1562.
- Efsing, P., Pettersson, K., 1996. The influence of temperature and yield strength on delayed hydride cracking in hydrided Zircaloy-2. In: Bradley, E.R., Sabol, G.P. (Eds.), *Zirconium in the Nuclear Industry: eleventh International Symposium*, ASTM STP 1295, American Society for Testing and Materials, pp. 394–404.
- Efsing, P., Pettersson, K., 2000. Delayed hydride cracking in irradiated Zircaloy cladding. In: Sabol, G.P., Moan, G.D. (Eds.), *Zirconium in the Nuclear Industry: twelfth International Symposium*, ASTM STP 1354, American Society for Testing and Materials, West Conshohocken, PA, pp. 340–355.
- Eshelby, J.D., 1957. The determination of the elastic field of an ellipsoidal inclusion and related problems. *Proceedings of the Royal Society, London A* 241, 376–396.
- Forsberg, K., Massih, A.R., 1990. Redistribution of hydrogen in Zircaloy. *Journal of Nuclear Materials* 172, 130–134.
- Grossbeck, M.L., Birbaum, H.K., 1977. Low temperature hydrogen embrittlement of Niobium II—microscopic observations. *Acta Metallurgica* 25, 135–147.
- Hagman, D.L., Reymann, G.A., Mason, R.E. (Eds.), *MATPRO version 11, A Handbook of Materials Properties for Use in the Analysis of Light Water Reactor Fuel Rod Behavior*, NUREG/CR-0479, TREE-1280, Rev 2, Department of Energy Publication.
- Huang, F.H., 1993. Brittle-fracture potential of irradiated Zircaloy-2 pressure tubes. *Journal of Nuclear Materials* 207, 103–115.
- Huang, F.H., Mills, W.J., 1991. Delayed hydride cracking behavior for Zircaloy-2 tubing. *Metallurgical Transactions A* 22A, 2049–2060.

- Hutchinson, J.W., 1968. Plastic stress and strain fields at a crack-tip. *Journal of the Mechanics and Physics of Solids* 16, 337–347.
- Kearns, J.J., 1967. Terminal solubility and partitioning of hydrogen in the alpha phase of zirconium, Zircaloy-2 and Zircaloy-4. *Journal of Nuclear Materials* 22, 292–303.
- Lee, J.K., Earmme, Y.Y., Aaronson, H.I., Russell, K.C., 1980. Plastic relaxation of the transformation strain energy of a misfitting spherical precipitate: ideal plastic behavior. *Metallurgical Transactions A* 11A, 1837–1846.
- Li, J.C.M., Oriani, R.A., Darken, L.S., 1966. The thermodynamics of stressed solids. *Zeitschrift für Physikalische Chemie Neue Folge* 49, 271–290.
- Lufrano, J., Sofronis, P., 2000. Micromechanics of hydride formation and cracking in zirconium alloys. *CMES* 1 (2), 119–131.
- Lufrano, J., Sofronis, P., Birnbaum, H.K., 1996. Modeling of hydrogen transport and elastically accommodated hydride formation near a crack-tip. *Journal of the Mechanics and Physics of Solids* 44 (2), 179–205.
- Lufrano, J., Sofronis, P., Birnbaum, H.K., 1998. Elastoplastically accommodated hydride formation and embrittlement. *Journal of the Mechanics and Physics of Solids* 46 (9), 1497–1520.
- Malvern, L.E., 1969. *Introduction to the Mechanics of a Continuous Medium*. Prentice-Hall, Englewood Cliffs, NJ.
- Marino, G.P., 1972. A numerical calculation of the redistribution of an interstitial solute in a thermal gradient. *Nuclear Science and Engineering* 49, 93–98.
- Markowitz, J.M., 1961. The thermal diffusion of hydrogen in alpha-delta Zircaloy-2. *Transactions of the Metallurgical Society of AIME* 221, 819–824.
- Massih, A.R., Rajala, T., Jernkvist, L.O., 1995. Analysis of pellet-cladding mechanical interaction behaviour of different ABB atom fuel rod designs. *Nuclear Engineering and Design* 156, 383–391.
- Needleman, A., 1987. A continuum model for void nucleation by inclusion debonding. *Journal of Applied Mechanics* 54, 525–531.
- Nelson, H.G., Williams, D.P., Stein, J.E., 1972. Environmental hydrogen embrittlement of an α - β titanium alloy: effect of microstructure. *Metallurgical Transactions* 3, 469–475.
- Northwood, D.O., Kosasih, U., 1983. Hydrides and delayed hydrogen cracking in zirconium and its alloys. *International Metals Reviews* 28 (2), 92–121.
- Peisl, H., 1978. Lattice strains due to hydrogen in metals. In: Alefeld, G., Volkl, J. (Eds.), *Hydrogen in Metals I. Basic Properties*. Springer, New York, pp. 53–74.
- Povirk, G.L., Needleman, A., Nutt, S.R., 1990. An analysis of residual stress formation in whisker-reinforced Al-SiC composites. *Materials Science and Engineering A* 125, 129–140.
- Puls, M.P., 1981. The effects of misfit and external stresses on terminal solid solubility in hydride-forming metals. *Acta Metallurgica* 29, 1961–1968.
- Puls, M.P., 1984. Elastic and plastic accommodation effects on metal-hydride solubility. *Acta Metallurgica* 32 (8), 1259–1269.
- Rice, J.R., 1968. Mathematical analysis in the mechanics of fracture. In: Liebowitz, H. (Ed.), *Fracture: An Advanced Treatise*, Vol. II. Academic Press, New York, pp. 191–311.
- Rice, J.R., Johnson, M.A., 1970. The role of large crack-tip geometry changes in plane strain fracture. In: Kanninen, M.F., Adler, W.F., Rosenfield, A.R., Jaffee, R.I. (Eds.), *Inelastic Behavior of Solids*. McGraw-Hill, New York, pp. 641–672.
- Sawatzky, A., 1960. Hydrogen in Zircaloy-2: its distribution and heat of transport. *Journal of Nuclear Materials* 2 (4), 321–328.
- Sawatzky, A., Vogt, E., 1963. Mathematics of the thermal diffusion of hydrogen in Zircaloy-2. *Transactions of the Metallurgical Society of AIME* 227, 917–928.
- Senkov, O.N., Dubois, M., Jonas, J.J., 1996. Elastic moduli of titanium-hydrogen alloys in the temperature range 20°C to 1100°C. *Metallurgical and Materials Transactions A* 27A, 3963–3970.
- Shewmon, P.G., 1989. *Diffusion in Solids*. The Minerals, Metals & Materials Society, Warrendale, Pennsylvania.
- Shi, S.-Q., Puls, M.P., 1994. Criteria for fracture initiation at hydrides in zirconium alloys I. Sharp crack-tip. *Journal of Nuclear Materials* 208, 232–242.

- Shih, D.S., Robertson, I.M., Birnbaum, H.K., 1988. Hydrogen embrittlement of α titanium: in situ TEM studies. *Acta Metallurgica* 36, 111–124.
- Simpson, L.A., Nuttall, K., 1977. Factors controlling hydrogen assisted subcritical crack growth in Zr–2.5Nb alloys. In: Lowe Jr., A.L., Parry G.W. (Eds.), *Zirconium in the Nuclear Industry*, ASTM STP 633, American Society for Testing and Materials, pp. 608–629.
- Simpson, L.A., Puls, M.P., 1979. The effect of stress, temperature and hydrogen content on hydride-induced crack growth in Zr–2.5Pct Nb. *Metallurgical Transactions A* 10A, 1093–1105.
- Sofronis, P., McMeeking, R.M., 1989. Numerical analysis of hydrogen transport near a blunting crack-tip. *Journal of the Mechanics and Physics of Solids* 37, 317–350.
- Takano, S., Suzuki, T., 1974. An electron-optical study of β -hydride and hydrogen embrittlement of vanadium. *Acta Metallurgica* 22, 265–274.
- Truesdell, C., Toupin, R., 1960. The classical field theories. In: Flugge, S. (Ed.), *Encyclopedia of Physics*, Vol. 3/1. Springer, Berlin, pp. 226–793.
- Tvergaard, V., Hutchinson, J.W., 1992. The relation between crack growth resistance and fracture process parameters in elastic–plastic solids. *Journal of the Mechanics and Physics of Solids* 40, 1377–1397.
- Varias, A.G., 1998a. Mathematical model for hydrogen diffusion, energy flow and hydride formation in zirconium under stress. Report BR-04-10-98, Solid Mechanics Research Office, Athens.
- Varias, A.G., 1998b. Constraint effects during stable transient crack growth. *Computational Mechanics* 21, 316–329.
- Varias, A.G., 1999a. Simulation of hydride formation and fracture in LWR fuel cladding—hydride precipitation ahead of a crack in a plate under tensile stress and temperature gradient (Task 3). Report BR-08-10-99, Solid Mechanics Research Office, Athens.
- Varias, A.G., 1999b. Simulation of hydride formation and fracture in LWR fuel cladding—tests of the finite element code (Task 2). Report BR-04-04-99, Solid Mechanics Research Office, Athens.
- Varias, A.G., Massih, A.R., 1999. Simulation of hydride formation and fracture in zirconium alloys. In: Wunderlich, W. (Ed.), *Proceedings of the European Conference on Computational Mechanics*. Munich, Germany.
- Varias, A.G., Massih, A.R., 2000a. Simulation of hydrogen embrittlement in zirconium alloys under stress and temperature gradients. *Journal of Nuclear Materials* 279 (2–3), 273–285.
- Varias, A.G., Massih, A.R., 2000b. Temperature and constraint effects on hydride fracture in zirconium alloys. *Engineering Fracture Mechanics* 65 (1), 29–54.
- Varias, A.G., Massih, A.R., 2000c. Numerical modeling of delayed hydride cracking in zirconium alloys. In: Miannay, D., Costa, P., Francois, D., Pineau, A. (Eds.), *Advances in Mechanical Behaviour, Plasticity and Damage*, Vol. 2. Elsevier Science, Oxford, pp. 1219–1224.
- Varias, A.G., Massih, A.R., 2001. Material degradation and fracture in zirconium alloys. In: Matzen, V.C., Tung, C.C.D. (Eds.), *Transactions of the 16th International Conference on Structural Mechanics in Reactor Technology*, Washington, DC, USA.
- Varias, A.G., O'Dowd, N.P., Asaro, R.J., Shih, C.F., 1990. Failure of bimaterial interfaces. *Materials Science and Engineering A* 126, 65–93.
- Wäppling, D., Massih, A.R., Ståhle, P., 1998. A model for hydride-induced embrittlement in zirconium-based alloys. *Journal of Nuclear Materials* 249, 231–238.